Mineralium Deposita (2024) 59:627–654
https://doi.org/10.1007/s00126-023-01220-9

ARTICLE

A modified paleoplacer model for the metaconglomerate-hosted gold deposits at Jacobina, Brazil

Enzio Garayp[1] · **Hartwig E. Frimmel**[1,2]

Received: 29 December 2022 / Accepted: 16 September 2023 / Published online: 25 October 2023

Abstract

Evidence is presented that the metaconglomerate-hosted Jacobina gold deposits in Brazil represent paleoplacers that became partly remobilized during later metamorphic overprint analogous to Witwatersrand-type deposits elsewhere, notably in South Africa. This includes strong lithological and sedimentological control on the gold, presence of detrital minerals with gold inclusions, and detrital gold particles. Detrital, synsedimentary, and post-depositional pyrite types can be differentiated. Whereas the first two types can be linked to gold accumulation, the latter was associated with gold dispersion. Synsedimentary pyrite has the highest Au content, from which elevated Au concentrations in Archean rivers can be inferred. The nature and extent of post-depositional alteration, mainly in the course of the Paleoproterozoic Orogeny, distinguishes the Jacobina deposits from other Witwatersrand-type gold deposits. Phase equilibria and Zr-in-rutile thermometry indicate peak metamorphic temperatures of ca. 600 °C. Both Mg-chlorite and Fe-chlorite formed in disequilibrium at approximately 280–340 °C during retrograde metamorphism. An igneous signature in the chemistry of some of the tourmaline and the remobilization of gold associated with Fe-oxides, near intrusive rocks, point at a local magmatic influence on the post-depositional mineralization stage. Whether magmatic hydrothermal fluids added Au to the system at that stage remains to be determined. Remobilization during regional metamorphism was insufficient to form substantial ore bodies but led to purification of the initially detrital gold particles that now contain relatively little Ag and Cu and lack Hg.

Keywords Jacobina · Gold · Quartz-pebble metaconglomerate · Placer · Metamorphism · Remobilization

Introduction

The metaconglomerate-hosted Jacobina gold deposits are located within the Bahia State, eastern Brazil (Fig. 1A). The deposits have been known since the eighteenth century and were mined episodically on a small scale for more than 200 years. Despite the long history, the first comparison with the famous Witwatersrand goldfields in South Africa was published in the English literature only in the late 1950s, when the Cold War triggered a global search for uranium (e.g., White 1956; Davidson 1957; Bateman 1958).

The Jacobina ores have never proved economic for uranium, but high Au grades attracted the attention of major gold miners. As a result, in the early 1970s the Anglo American South Africa Corporation implemented the first systematic gold exploration program in the area and revealed the economic potential of Jacobina. The program warranted an industrial-scale processing plant that produced over 20 t of Au between 1983 and 1998 (Pearson and Tagliamonte 2005). More recently, Yamana Gold Inc. operated the Jacobina mines but was taken over by the Canadian Pan American Silver Corp in 2023. Yamana reported total estimated proven and probable reserves of ca. 77 t of Au at an average grade of 2.27 g/t and, in addition, ca. 95 t of Au as measured and indicated resources at similar grade with extension at greater depth not constrained as yet (http://www.panamericansilver.com, http://www.yamana.com).

The first publications on Jacobina reflected the controversy on the metallogenesis of the Witwatersrand ores at the

Editorial handling: A. R. Cabral

✉ Enzio Garayp
enzio.garayp@stud-mail.uni-wuerzburg.de

[1] Department of Geodynamics and Geomaterials Research, Bavarian Georesources Centre, Institute of Geography and Geology, University of Würzburg, Am Hubland, 97074 Würzburg, Germany

[2] Department of Geological Sciences, University of Cape Town, Rondebosch 7701, South Africa

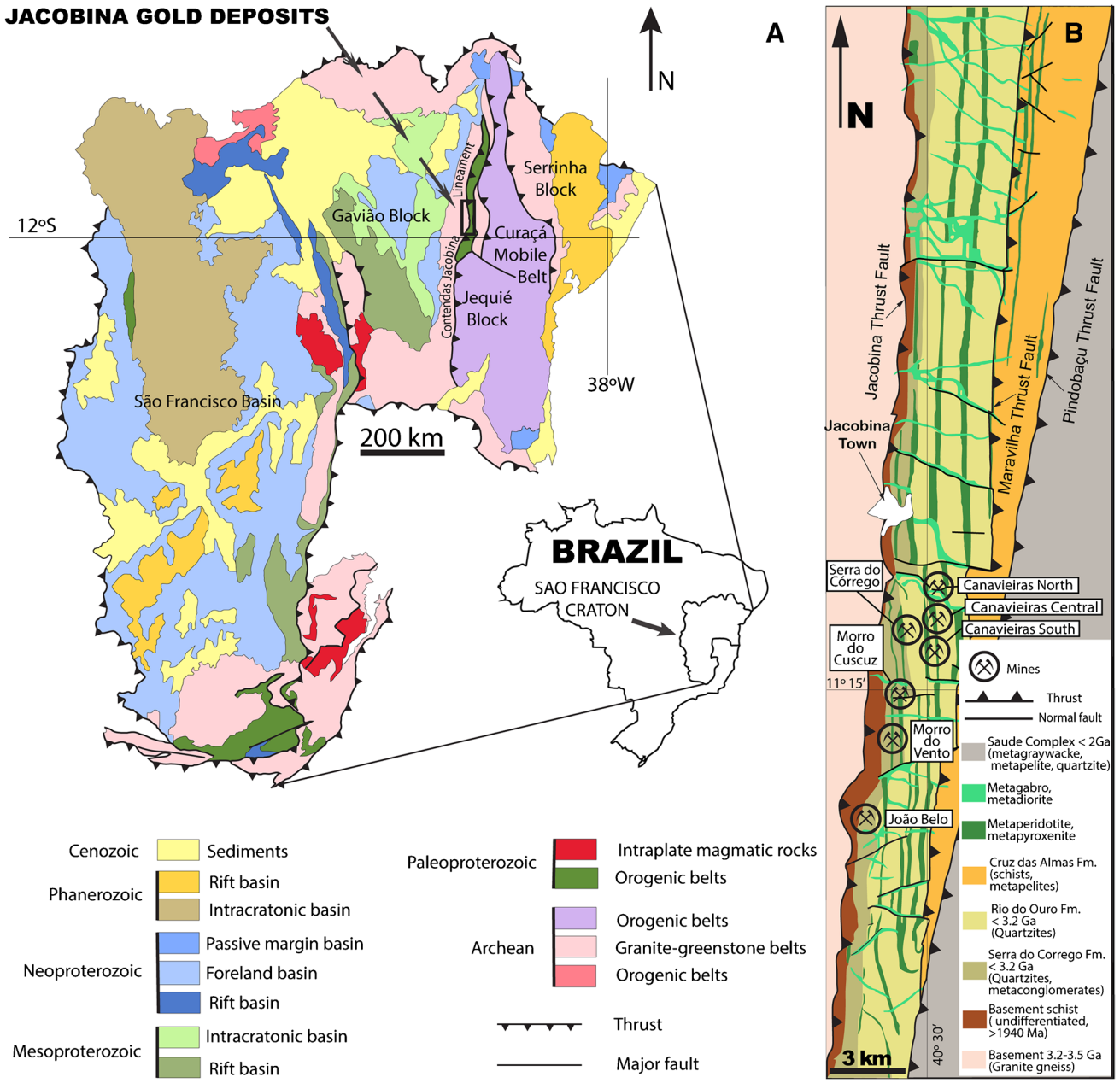

Fig. 1 A—Location of the Jacobina gold deposits in the São Francisco Province, Brazil (modified from Delgado et al. 2003). B—Geological map of Jacobina Mine area (modified from Couto et al. 1978). Geochronological information from Milesi et al. (2002), Teles et al. (2015), Zincone et al. (2017)

time. Initially, the discussion was polarized between a syngenetic placer (Bateman 1958) and an epigenetic hydrothermal model (White 1956; Davidson 1957). Later, these ideas evolved into the modified paleoplacer model, as adopted by most researchers for the Witwatersrand deposits, suggesting local remobilization of detrital gold by post-depositional fluids (Cox 1967; Gross 1968). This mimicked the debate on the Witwatersrand deposits for which a modified paleoplacer model (e.g., Minter 1999; Frimmel and Minter 2002; Frimmel et al. 2005) and various epigenetic hydrothermal models had been promoted (Barnicoat et al. 1997; Phillips and Law 2000). Presently, the modified paleoplacer model is favored by most geoscientists (for a summary of arguments against an epigenetic formation of the Witwatersrand ores see Frimmel and Nwaila 2020).

Post-depositional alteration is ubiquitous in Jacobina, which prompted some authors to propose composite models like the "hydrothermal shear reservoir" (Milesi et al. 2002) or an altogether epigenetic origin of the gold (Ledru et al. 1997; Teixeira et al. 2001, 2010, 2019). Recently, Teles et al.

(2020), based on S isotopes and trace elements, compared the Jacobina pyrites with those in the Witwatersrand and suggested similarities with the modified paleoplacer model. In the present study we look at the sedimentological features and the mineral paragenesis of the Jacobina gold deposits, which support the strong similarities with the pyritic metaconglomerate-hosted Witwatersrand deposits. We also reassess the post-depositional alteration at Jacobina and focus on the morphology, chemical variability, and geothermometry of key minerals based on which a metallogenetic model for these deposits is developed.

Geological setting

The Jacobina gold deposits are hosted by a thick siliciclastic succession exposed in a series of north–south oriented ridges along a strike-length of some 200 km. These ridges protrude up to 650 m above the surrounding plains and reach elevations of >1000 m above sea level at the highest peaks. The succession represents the fill of the Jacobina Basin. It is composed predominantly of quartzite with interlayered metaconglomerate beds near the base. The strata strike north–south and dip 40–70° to the east forming a hogback landscape with escarpments facing west and dip slopes facing east. Mafic and ultramafic sills and dikes as well as faults and shear zones underlie the subdued relief, forming the bottom of deep V–shaped valleys between the quartzitic ridges. The gold mined in Jacobina is hosted by metaconglomerate beds which are locally called reefs, a nomenclature inherited from the South African Witwatersrand mines. The gold deposits are exposed in the southwestern sector of the Jacobina Range and the main operations are known locally as Canavieiras North, Canavieiras Central, Canavieiras South, Serra do Córrego, Morro do Cuscuz, Morro do Vento, and João Belo mines (Fig. 1B).

The Jacobina Basin is located in the São Francisco Craton (Almeida 1977, 1981), more specifically at the eastern edge of the Gavião Block, one of the Archean blocks that constitute the cratonic shield areas (Fig. 1A). As such, the basin is enclosed by the oldest terranes in South America, including the 3.65 Ga Mairi Gneiss Complex, 3.4 Ga tonalite-trondhjemite-granodiorite (TTG) suite, 3.3 Ga granite and associated felsic volcanic rocks, and supracrustal rocks including greenstone belts (Nutman and Cordani 1993; Mascarenhas and Silva 1994; Magee et al. 2001; Barbosa and Sabaté 2004; Teles et al. 2015; Zincone et al. 2016; Oliveira et al. 2020; Moreira et al. 2022). The eastern boundary of the Gavião Block is defined by the Contendas-Jacobina Lineament, a major suture zone formed during the ca. 2.0 Ga Paleoproterozoic Orogeny when the Gavião Block collided with two other Archean blocks from the east, the Serrinha Block to the north and the Jequié Block to the south (Fig. 1A). Late- to post-tectonic peraluminous granitic bodies are widespread along the Contendas-Jacobina Lineament for about 500 km (Sabaté et al. 1990). In addition, the Jacobina Group hosts different generations of igneous rocks, which vary from ultramafic, mafic to intermediate sills and dikes. A N-S striking group of sills and dikes consists of amphibolite, serpentinites, metapyroxenite, and metaperidotite, whereas a younger E-W to NW–SE striking group, consisting of mainly metagabbro and metadiorite, crosscuts the former (Leo et al. 1964; Couto et al. 1978; Santos 2011; Teixeira 2017; Reis et al. 2021 and references therein).

The N-S elongated shape of the Jacobina Basin is a product of east–west transpressive shortening associated with the Paleoproterozoic Orogeny (Fig. 1B). Ledru et al. (1997) documented the deformation in mineralized metaconglomerates around Jacobina town and described westward thrusts, reverse faults, and associated sinistral transcurrent kinematic movements. More recently, Dos Santos et al. (2019), using gravimetric modeling, confirmed the tectonic framework for the southern segment of the Jacobina succession, for which they described major north-south striking shear zones and imbricated blocks developed in three compressive deformation phases. The first phase, which led to frontal stretch lineation, grain rotation, and S/C pairs, was predominantly transpressive with vergence to the west. The second phase, parallel to the first one, was characterized by wrench tectonics with subvertical left-lateral transcurrent faults, oblique stretching lineation, and asymmetrical folds with subvertical axes. The third, brittle phase was generally more prominent toward the east of the basin where micaschist and talcschist display a conspicuous north–south striking foliation. In the quartzite and metaconglomerate domains in the west, the foliation is not as penetrative as in the east, and strain was accommodated in more widely spaced shear zones.

Consensus prevails that the main metamorphic event that affected the Jacobina Basin fill is related to the Paleoproterozoic Orogeny (Ledru et al. 1997; Milesi et al. 2002; Barbosa and Sabaté 2004; Leite et al. 2007). The metamorphic mineral assemblage in the metaconglomerates, that is, quartz, muscovite or fuchsite, chlorite and, in places, pyrophyllite, is not very diagnostic of peak metamorphic conditions, because both chlorite and pyrophyllite are retrograde (see below). More informative are mineral assemblages recorded in metapelites higher up in the stratigraphy but still within the Jacobina Group. There the assemblages quartz-plagioclase-staurolite-biotite-sillimanite, andalusite-garnet-cordierite-biotite, and sillimanite-biotite-muscovite have been reported, from which Milesi et al. (2002) deduced peak metamorphic conditions between 500 and 600 °C at 4.5 to 5.0 kb. This was further constrained by Leite et al. (2007), who calculated peak metamorphic temperatures between 560 and 600 °C based on garnet-chlorite and garnet-staurolite geothermometry. Ledru et al. (1994, 1997) described

andalusite porphyroblasts synchronous with the foliation and locally as replacement of, or overgrowths on, kyanite, which, in combination with the above, points at a clockwise P–T path through the lower amphibolite facies P-T field. Teixeira et al. (2001) mentioned syn- to late-tectonic poikiloblasts of andalusite and fibrolite, both parallel to the main foliation, in the matrix of the metaconglomerates, which corroborates the peak metamorphic conditions estimated for the metapelites above. In addition, the mafic and ultramafic dikes and sills reveal some of the metamorphic/alteration history in the area. Mafic rocks in the form of amphibolite mirror the peak metamorphic conditions estimated above, with some retrograde greenschist-facies alteration of hornblende to actinolite. The ultramafic rocks occur in the form of talc-tremolite fels, derived from original pyroxenite. The mineral assemblage therein, that is, tremolite–talc–chlorite–carbonate–pyrite–chalcopyrite–hematite (Santos 2011), reflects retrograde hydrothermal overprint under similar P–T but oxidizing conditions.

The age of the Paleoproterozoic Orogeny in the Jacobina area has been constrained by Ar^{40}-Ar^{39} ages between 1943 ± 13 and 1912 ± 13 Ma, obtained on synkinematic micas in Jacobina shear zones, thus providing a minimum age on metamorphism (Ledru et al. 1997). These authors also dated post-kinematic muscovite and biotite 30 km north of Jacobina around the Caraíba granite at 1911 ± 13 Ma and 1903 ± 13 Ma, respectively. Late- to post-tectonic granite with ages between 1970 and 1800 Ma (Teixeira et al. 2001) along the Contendas-Jacobina Lineament mark the final stages of continental collision.

Detrital zircon geochronology constrained the source of the Jacobina sediments as Paleoarchean, with ages ranging between 3251 ± 52 and 3614 ± 67 Ma and age peaks between 3.3 and 3.4 Ga (Teles et al. 2015). These data confirmed previous U–Pb detrital zircon ages of 3440 to 3320 Ma (Mougeot et al. 1996; Magee et al. 2001). Thus, based on the youngest ages obtained by Teles et al. (2015), the maximum age of Jacobina sediment deposition is 3.3 Ga. The minimum age of deposition remains, however, poorly constrained. Based on the presence of detrital pyrite in the matrix of the metaconglomerates, sedimentation should be older than the global Great Oxidation Event (Teles et al. 2015, 2020), estimated at ca. 2.4 Ga (Holland 2006; Farquhar et al. 2011).

Importantly, the study by Teles et al. (2015) revealed a conspicuous lack of Paleoproterozoic zircon grains, thus challenging a previous notion that the maximum depositional age of the Jacobina sediments is as young as 2086 Ma (Mougeot et al. 1996; Ledru et al. 1994, 1997; Milesi et al. 2002). The latter constraint was obtained on detrital zircon grains from the Saúde Complex, a younger supracrustal succession that became tectonically juxtaposed to the Jacobina Group. This argument was corroborated by Zincone et al. (2017) who determined the maximum depositional age of the Saúde Complex as 2050 ± 16 Ma and showed that it was probably deposited in a foreland basin not related to the Jacobina Basin at all.

The work by Zincone et al. (2017) has clarified another important point concerning the tectonic setting of the Jacobina Basin. In the past, both the Jacobina Group and the Saúde Complex were considered part of the same foreland basin (Ledru et al. 1994, 1997; Milesi et al. 2002)—a concept that contradicted previously proposed rifting models (Mascarenhas et al. 1992; Mascarenhas and Silva 1994; Horscroft et al. 2011). However, Zincone et al. (2016) recognized intraplate magmatic systems that represent the initial stage of intra-continental rifting geographically associated with the Jacobina Basin. They also pointed out the close age relationship between felsic rift magmatism and the detrital zircon ages available for Jacobina and concluded that a vast volcanic-plutonic system fed into the Jacobina Basin. Thus, the source of the Jacobina sediments most likely includes a combination of >3.4 Ga TTG suites, younger (3.3 Ga) non-TTG high-silica rhyolite and granite, and supracrustal rocks, including Archean greenstones.

The stratigraphy of the Jacobina Group was recently reviewed by Reis et al. (2021), who proposed its subdivision into four formations, from the bottom: Serra do Córrego, Rio do Ouro, Cruz das Almas, and Fazenda Bananeira. In the present study our focus is on the two lowermost units, the Serra do Córrego Formation and the overlying Rio do Ouro Formation, in which primary sedimentary features are preserved and exposed by extensive exploration and mining works on surface and underground, (e.g., Couto et al. 1978; Molinari and Scarpelli 1988; Mascarenhas et al. 1998; Pearson et al. 2005). The Serra do Córrego Formation, host of the Jacobina deposits, is exposed for 85 km (Pearson et al. 2005) on the western margin of the basin where it unconformably lies on Archean granitic basement. It comprises mainly coarse-grained quartzite interlayered with oligomictic metaconglomerate and pebbly quartzite. Pebbles consists predominantly of quartz and minor chert and vary in size from small to very large (4–64 mm). The Serra do Córrego Formation varies in thickness between 500 and 1000 m and is divided into three units, from the base to the top: Lower Conglomerate, Intermediate Quartzite, and Upper Conglomerate (Molinari and Scarpelli 1988, Fig. 2). Minter (1975) and Strydom and Minter (1976) used paleocurrent analysis, isopach maps and pebble size data to conclude that the sediments were eroded from the east, transported to the west by braided streams and deposited onto a large wet alluvial fan.

The up to 2 km thick Rio do Ouro Formation is composed mainly of orthoquartzite, which is finer grained and shows greater lateral extent than the lower Serra do Córrego Formation. The transition between the two formations is gradational (Minter 1975). Based on a substantial

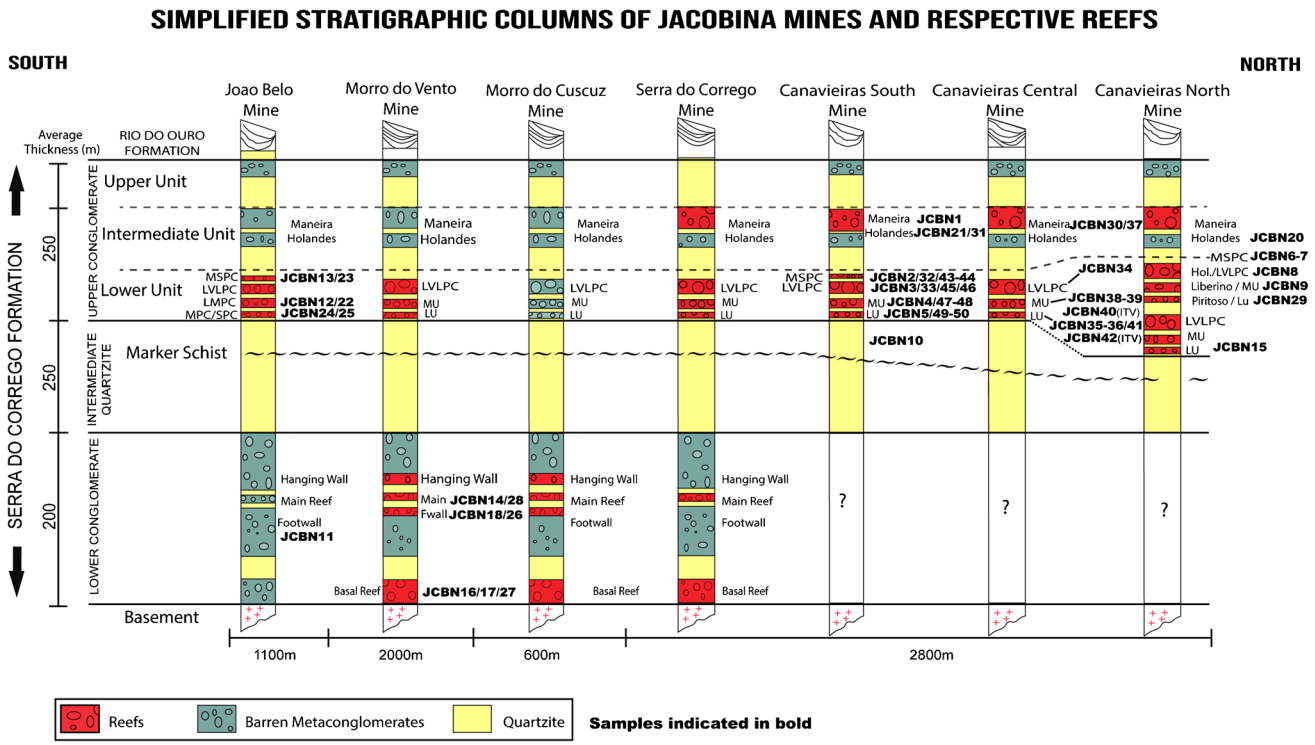

Fig. 2 Stratigraphy of the Serra do Córrego Formation and associated reefs (modified from Soares et al. 2020). Note that samples are indicated in bold

change in the paleocurrent direction and associated primary sedimentary structures, which include small-scale trough cross bedding and asymmetrical and oscillation ripple marks, the upwards fining Rio do Ouro Formation can be interpreted as a marine overlap on the alluvial Serra do Córrego Formation (Minter 1975; Molinari and Scarpelli 1988). In the Rio do Ouro Formation, gold occurs locally in uneconomic quartz veins. Pearson et al. (2005) referred to several of these small gold occurrences as altered shear zones. More recently, Miranda et al. (2021) studied some of these occurrences using mineral chemistry and fluid inclusion microthermometry and concluded that the occurrences are related to major reverse faults associated with the Paleoproterozoic Orogeny. This tectonism-related style of mineralization is sparsely distributed along the whole belt, predominantly on the northeastern section between 20 and 60 km north of the Jacobina mines, where thrust structures prevail (Teixeira et al. 2001; Pearson et al. 2005; Miranda et al. 2021). Gold also occurs associated with mafic/ultramafic dikes, a feature that has been reported by all previous authors who studied Jacobina gold. These occurrences are, however, only local and substantially smaller than the principal mineralization in the metaconglomerate units.

The sedimentological control on the gold mineralization

The bulk of the gold in Jacobina is hosted by metaconglomerates and subordinately pebbly quartzite. These sedimentary units form laterally extensive stratiform orebodies that extend for several kilometers along strike and on dip at different stratigraphic levels of the Serra do Córrego Formation. Soares et al. (2020) recognized at least 15 reefs in the lower 700 m of that formation (Fig. 2). Mine sections based on diamond drilling show that some of the reefs extend for > 1 km on dip and remain open at depth (Molinari and Scarpelli 1988; Pearson et al. 2005; Fig. 3). In the early days of exploration, Minter (1975) mapped the Main Reef as a continuous sedimentary unit composed of small-pebble metaconglomerate in quartzite that extended for > 3 km along strike. Pearson et al. (2005) also pointed out that mineralized zones show distinct plunges that correspond to fluvial channels. This close relationship between gold and primary sedimentary features represents a remarkable control on mineralization that, like in the Witwatersrand, has guided explorers and miners since the beginning of mining operations. For instance, the mineralization potential of the Upper Conglomerate in Jacobina was predicted based on the

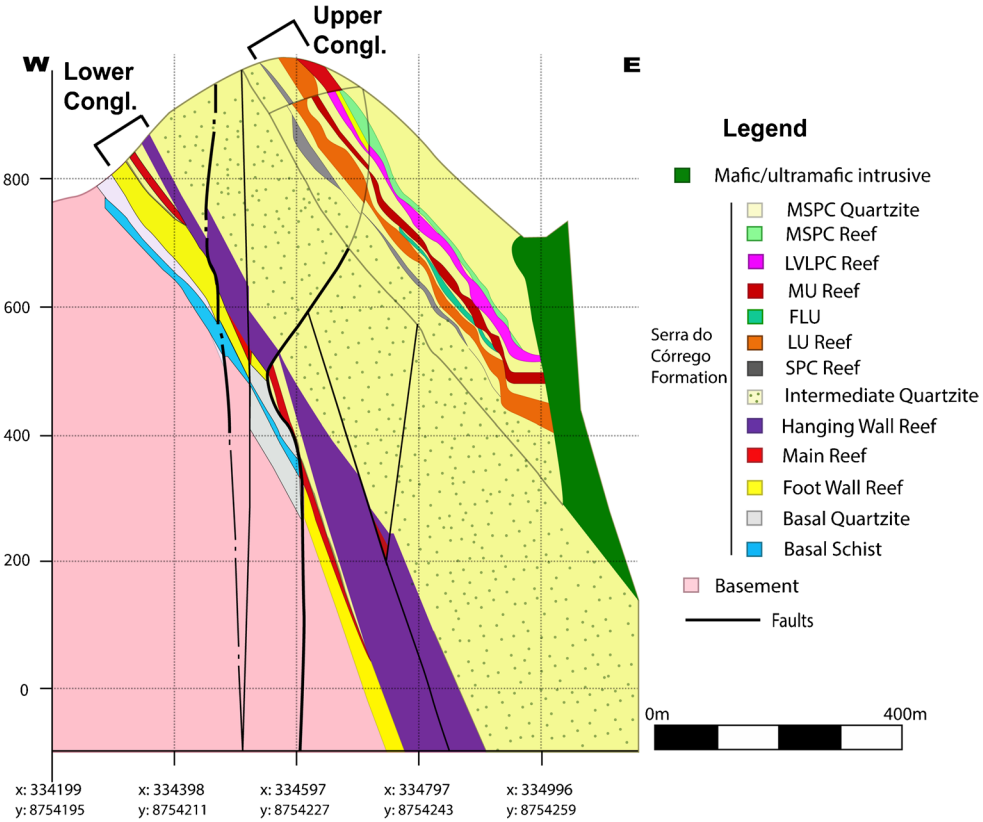

Fig. 3 Geological section of the Morro do Vento area based on surface and underground drilling (modified from Soares et al. 2020)

sedimentological nature of the Lower Conglomerate (Minter 1975) only to be confirmed later (Molinari and Scarpelli 1988), revealing the largest resources in the Jacobina district.

The main mineralized zones consist of a series of discrete gold and heavy mineral-enriched increments just a few centimeters to a few meters thick, which are intercalated with barren intervals. This alternation adds up to hundreds of meters in thickness, thus forming large-scale mineralized zones. In many cases, gold accumulated on sedimentary unconformities. A close association with sedimentary structures on a meso-scale is also evident by a strong correlation between Au grade and small-pebble beds, the most densely packed metaconglomerates, or the bottom of large-pebble metaconglomerate beds deposited at the base of channels (Minter 1975; Hendrickson 1984). When associated with smaller pebble layers, gold tends to be associated with cross-bedded foresets or it is concentrated on small-pebble accumulations at the base of trough cross-bedded sets or cosets. This initial work by Minter (1975) and Hendrickson (1984) provided the best assessment of orebody geometry and showed that the reefs consist of large-scale sedimentary units. Unfortunately, this valuable work was not published in the scientific literature but documented in internal company reports (Minter 1975; Strydom and Minter 1976) and in a thesis (Hendrickson 1984). Consequently, the paleoplacer concept has not been explored to its full potential. Any assessment of the Jacobina gold mineralization should, therefore, consider a possible placer origin. In the present study we provide further evidence of detrital gold as inclusions in quartz pebbles and in detrital pyrite grains, as well as round, evidently detrital, gold clasts, all preserved in hydraulic-concentrated heavy mineral layers.

Sampling and analytical methodology

A total of 74 polished thin sections from 12 different reefs were prepared from samples collected in various locations including surface outcrops, underground exposures, and drill core (down to 600 m depth), in order to obtain the best coverage of the mine area at different depths (see Fig. 2 and online supplementary material ESM Table 1 for sample location). Following petrography, electron microprobe analyses (EMPA) were conducted to assess the composition of chlorite, tourmaline, rutile, and gold, and laser-ablation inductively coupled plasma mass spectrometry (LA-ICPMS) to determine the trace element contents of pyrite. Both techniques were applied to in-situ mineral grains in polished thin sections of gold-mineralized samples.

EMPA was conducted at the Department of Geodynamics and Geomaterials Research, University of Würzburg, using a JEOL JXA 8800L superprobe with 4 wavelength-dispersive spectrometers. For chlorite, tourmaline, and rutile, the measuring conditions were set at 15 kV accelerating voltage, 20 nA beam current, and a beam diameter of 5 µm for chlorite and tourmaline and 1 µm for rutile. TAP (Na; Mg, Al, Si, As), PET (Ca, K, S, Ti, Cr, Ba, Pb), and LIF (Mn, Fe, Co, Ni, Zn) monochromator crystals were used for rutile and chlorite, and TAP (F, Na, Mg, Al, Si), PET (Ca, Ti, Cr, Pb, Bi), and LIF (Mn, Fe, Cu, Zn) for tourmaline. After ZAF matrix correction, the analytical errors were estimated at < 1% and the detection limits at 0.05 wt%, except for Zr in rutile for which the detection limit was calculated as 160 ppm.

The EMPA gold analyses measured the following elements: Au, Ag, Hg, Cu, and Pd. Measurement conditions were 20 kV accelerating voltage, 40 nA beam current, 2 µm beam diameter. A LIF crystal was used for Au, Hg, Cu, and a PET crystal for Ag and Pd, with counting times of 20 s for Au and 30 s for the other elements. Pure Au, Ag, Pd, Cu, and HgS were used as standards. The ZAF matrix correction procedure was applied to calculate the concentrations from characteristic X-ray lines; Lα for Au, Ag, Hg, and Pd, and Kα for Cu. Analytical errors are < 1% and the detection limit was 0.05 wt%.

The LA-ICPMS analyses were conducted at the Lithosphere Dynamics Section of the Geo-Center of Northern Bavaria, Erlangen, using a QICP-MS Agilent 7500c equipped with a UP193FX New Wave Research laser unit. Plasma power was set at 1300 W and the following gases were used: He (0.5 l/min) and Ar (1.15 l/min) as carrier gases I and II, respectively, Ar (14.9 l/min) as plasma gas and Ar (0.9 l/min) as auxiliary gas. A total of 18 elements were analyzed, namely, Ag, As, Au, Cd, Co, Cu, Hg, Ir, Mo, Ni, Os, Pb, Pd, Pt, Re, Rh, Ru, and Tl. External calibration was separated into three groups: Ru, Rd, Pd, Os, Ir, Pt, and Au contents were calculated based on reference material Po724 B2 SRM (Memorial University Newfoundland), that of Re based on reference material $(Fe, Ni)_{1-x}S$ (University of Münster), and those of Co, Ni, Cu, As, Mo, Ag, Cd, Hg, Tl, and Pb based on the USGS reference material MASS-1. The laser beam was fired at 16 Hz repetition rate for single spot size of 40 µm in diameter with 0.64 GW/cm^2 irradiance and 3.1 J/cm^2 fluence and 20-s background and 20-s analyses (time-resolved analyses). Interactive data reduction was performed using GLITTER version 4.4.4. Measuring times were set at 10 ms for ^{29}Si, ^{33}S, ^{34}S, ^{63}Cu, ^{65}Cu, 25 ms for ^{59}Co, ^{60}Ni, ^{75}As, ^{95}Mo, ^{97}Mo, ^{99}Ru, ^{101}Ru, ^{103}Rh, ^{105}Pd, ^{107}Ag, ^{108}Pd, ^{109}Ag, ^{111}Cd, ^{185}Re, ^{189}Os, ^{193}Ir, ^{195}Pt, ^{202}Hg, ^{205}Tl, and ^{208}Pb and 40 ms for ^{197}Au. Concentrations were obtained in ppm with 1 sigma error, 99% confidence level.

We calculated the formation temperature of chlorite and rutile in gold-mineralized samples. Chlorite thermometry has been extensively studied in the last decades and has proven to be an effective tool in specific situations, preferably alongside with complementary methods (e.g., De Caritat et al. 1993; Vidal et al. 2016; Inoue et al. 2018; and references therein). We used the empirical approach, which is the simplest chlorite thermometry method and serves the comparative purposes of this study. The method is based on the observation that Al^{IV} increases with temperature (Cathelineau and Nieva 1985; Cathelineau 1988; Kranidiotis and MacLean 1987; Hillier and Velde 1991; Zang and Fyfe 1995). The following empirical thermometers were used to approximate the formation temperature of chlorite: Cathelineau and Nieva (1985), Zang and Fyfe (1995), and El-Sharkawy (2000).

For rutile, the method used was Zr-in-rutile thermometry based on the interdependence of the Zr content in rutile and the formation temperature (Zack et al. 2004a, b; Watson et al. 2006), and to a lesser extent also pressure (Tomkins et al. 2007). The technique has been successfully used in various settings (e.g., Meinhold et al. 2008; Luvizotto and Zack 2009; Kooijman et al. 2012; Ewing et al. 2013; Pape et al. 2016), and Zack and Kooijman (2017) confirmed that temperatures obtained from Zr-in-rutile thermometry are good proxies for peak metamorphic temperatures of a given rutile population. The following Zr-in-rutile thermometers were applied: Zack et al. (2004b), Watson et al. (2006), and Tomkins et al. (2007). The mineral assemblage of the gold-mineralized metaconglomerates of Jacobina fulfills the basic requirements of the method, that is, SiO_2-saturation and equilibrium between quartz, zircon, and rutile (Zack et al. 2004a, b). The full set of analyses is presented online in ESM Tables 2, 3, 4, 5, 6.

The ore mineral assemblage and paragenesis

The mineralogical makeup of the host metaconglomerates comprises essentially detrital quartz and heavy minerals, including pyrite, zircon, rutile, uraninite, chromite, spinel, galena, ilmenorutile, tourmaline, molybdenite, magnetite, thorite, monazite, and gold. The metamorphic/hydrothermal assemblages include some of the allogenic minerals, such as quartz, pyrite, rutile, tourmaline, and gold but also neoformed minerals like muscovite/fuchsite, chlorite, pyrophyllite, hematite, goethite, brannerite, bornite, chalcopyrite, covellite, chalcocite, linnaeite, sphalerite, digenite, mackinawite, diaspore, phlogopite, pyrrhotite, and pentlandite, the last two as inclusions in pyrite (see also Hendrickson 1984; Ledru et al. 1997; Milesi et al. 2002). The color of the host rocks is determined by the relative mineral proportions and varies between shades of gray, green, red, and brown (Fig. 4). In terms of opaque minerals, the mine jargon refers

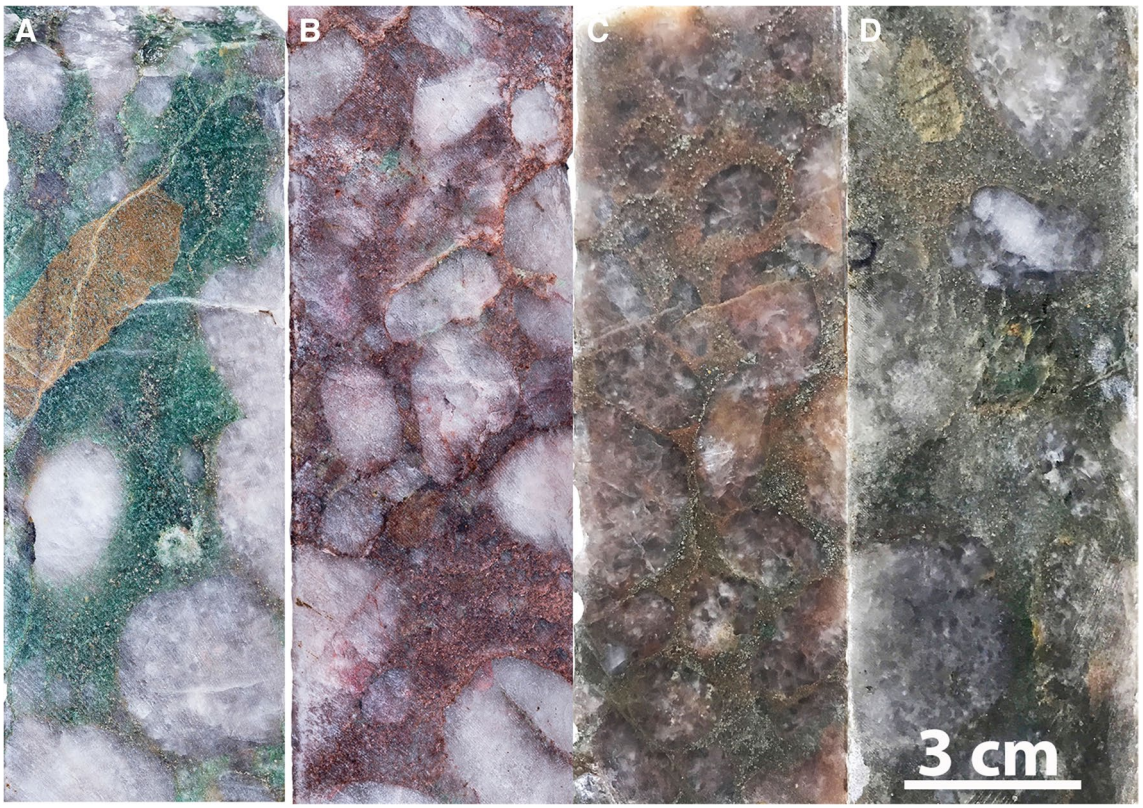

Fig. 4 Ore color variation in hand specimen controlled by mineral abundance. **A** Bright green from fuchsite. **B** Reddish matrix due to the presence of hematite. **C** Reddish-brown from iron oxides permeating grayish matrix and smoky quartz pebbles. **D** Greenish-gray tint produced by tourmaline. Pyrite appears in **A**, **C**, and **D** as fine bright yellowish spots

to two types of ore, the sulfide ore, in which pyrite is the dominant opaque mineral (Fig. 4D), and the oxidized ore, in which Fe-oxides and -hydroxides are predominant (Fig. 4B). The mineral assemblages depend not only on the respective host rock but also on the extent of retrograde overprint, such as in shear zones, and on the proximity to intrusive bodies, that is, mafic to ultramafic dikes and sills as well as granitoids. For instance, hematite and goethite are spatially related to the mafic/ultramafic intrusives (to be discussed below). A brief petrographic description of the most important minerals with their relevant role in the various stages of mineralization is presented below.

Silicates

Silicates are the main phases in the Jacobina metasedimentary rocks. Quartz is the most common, comprising > 90 vol%, mostly as detrital sand grains and pebbles. Undulatory extinction, subgrain boundaries and microfractures attest to some post-depositional stress on the larger quartz particles, whereas on smaller grains, grain boundary migration and local recrystallization indicate the effects of metamorphism. White mica and chlorite are minor minerals in the metaconglomerates, followed in abundance by zircon and tourmaline. White mica occurs as isolated sheets and aggregates up to 1 mm in size and varying in color from transparent to light blueish green (fuchsite). It also occurs interlayered with chlorite in equigranular aggregates (Fig. 5A and B). Two types of chlorite were identified. The most abundant, Chlorite 1, is interstitial in the matrix of the metaconglomerates as individual sheets

Fig. 5 Microphotographs of the main silicates in plane polarized light. **A** Muscovite (Mus, light green fuchsite variety) and chlorite (Chl, light brown, Chlorite 1) surrounded by quartz (colorless) sample JCBN36. **B** Same view as **A** under crossed polars. **C** Chlorite (olive green, Chlorite 2), goethite (Goe) in quartzitic matrix sample JCBN31. **D** Isolated tourmaline crystal (green) surrounded by quartz (colorless) sample JCBN2. **E** Tourmaline needles clustered in the center of the image surrounded by quartz (colorless) and goethite (reddish dark brown and black) sample JCBN17. **F** Tourmaline cluster (black) detailed in the microprobe screen shot at the bottom right, in quartzitic matrix sample JCBN38. **G** Rounded detrital zircon (pinkish—green high interference colors under crossed nicols) surrounded by quartzitic matrix sample JCBN17. **H** Brownish pyrophyllite (pyro) associated with fuchsite (fuch) in contact with pyrite (py) in quartzitic matrix sample JCBN46

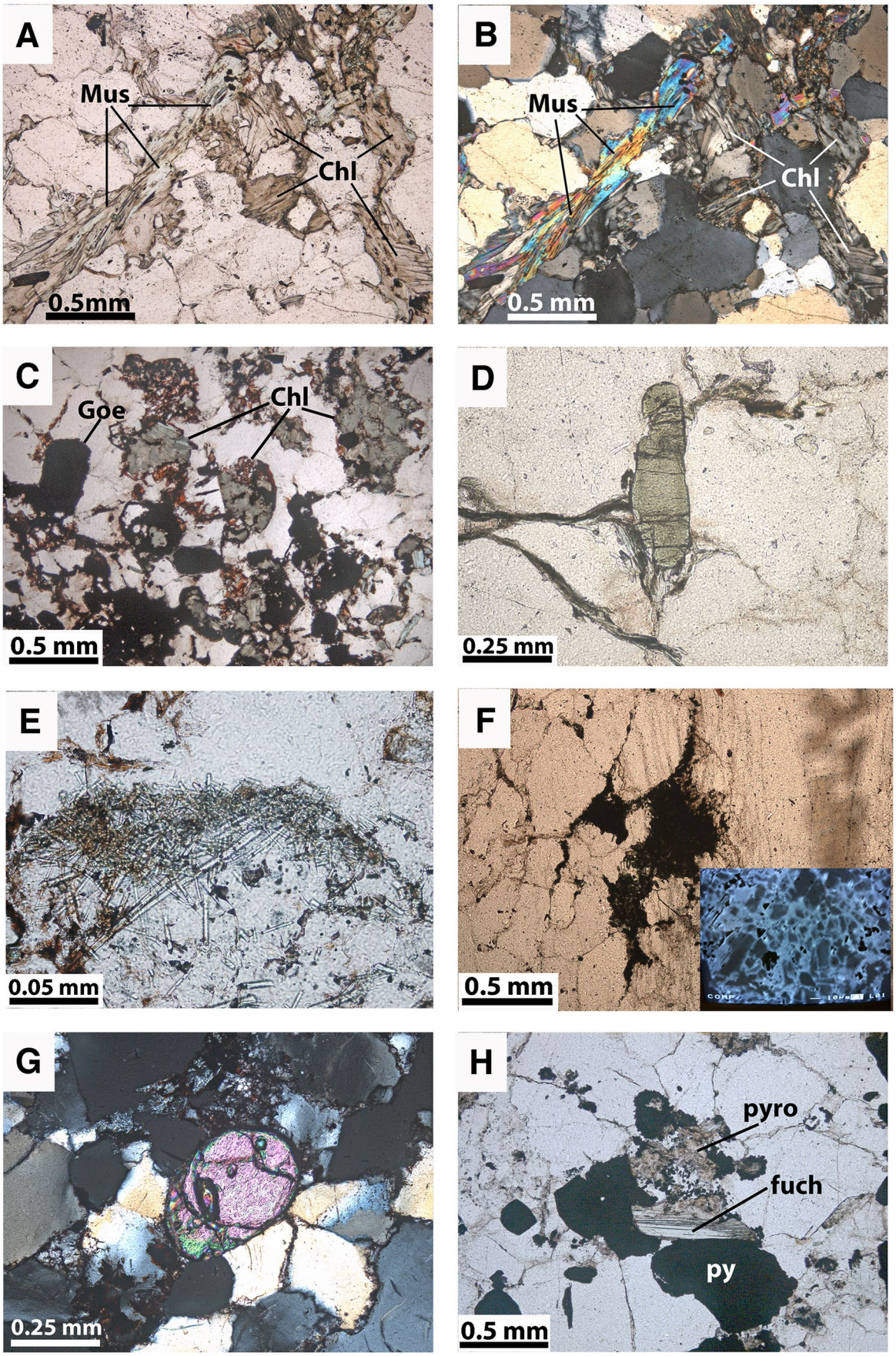
A
Mus
Chl
0.5mm
B
Mus
Chl
0.5 mm
C
Goe
Chl
0.5 mm
D
0.25 mm
E
0.05 mm
F
0.5 mm
G
0.25 mm
H
pyro
fuch
py
0.5 mm

and aggregates, varying in color from brown to olive-green (Figs. 5A, B, and 7A). The second type, Chlorite 2, occurs as dark green aggregates, which suggest pseudomorphs of a detrital mafic precursor (Fig. 5C). Tourmaline is present as euhedral to subhedral crystals either isolated or in clusters. Individual crystals are columnar (Fig. 5D) or acicular (Fig. 5E), reaching as much as 700 µm in length, or they are stubby (Fig. 5F). Tourmaline also forms tiny inclusions in various minerals, such as chlorite, muscovite, and quartz. Zircon occurs invariably as well-rounded grains between 50 and 500 µm in length (Fig. 5G), commonly associated with heavy-mineral layers. Pyrophyllite was identified only in two samples as alteration of fuchsite (Fig. 5H).

Sulfides

The sulfides identified in the present study include predominantly pyrite (2–5 vol%, in places as much as 50 vol%), minor galena, and traces of chalcopyrite, bornite, chalcocite, and siegenite. Pyrite occurs mostly as isolated grains from a few microns up to 3 mm in size, commonly concentrated in layers with other heavy minerals in the matrix of the metaconglomerates and in quartzites (Fig. 6A–C). In places, almost monomineralic layers of pyrite reflect the former accumulation of pyrite sands, as exemplified by sedimentary beds of pyrite intercalated with dark green pebbly quartzite of the Holandês Reef (Fig. 6A, B). Elsewhere, pyrite occurs as millimeter-sized grains within quartzitic matrix of clast-supported metaconglomerate (Fig. 6C).

On a microscopic scale, pyrite is described here based on two main aspects, the external morphology, which is derived from the outline of the particle in thin section, and its internal texture, that is, compact or porous. The term porous is used here in the sense of appearance as traditionally used in the Witwatersrand literature (e. g. Ramdohr 1955; Saager 1970; Hallbauer 1986; England et al. 2002; Hofmann et al. 2009; Koglin et al. 2010). Essentially, the porous texture consists of tiny, densely distributed inclusions and cavities that resemble pores under low magnification (Fig. 6D), whereas the compact texture is uniform or massive and contains only very few cavities and inclusions (Fig. 6E). The external morphology of the pyrite varies between anhedral and subhedral to well-rounded grains. Figure 6F illustrates a typical heavy mineral layer showing various morphological and textural types, from porous to compact round grains and angular fragments. Two morphological types stand out among round forms, the porous round pyrite and the compact round pyrite, both interpreted here as detrital, having acquired their rounding by abrasion during sediment transport (to be discussed in more detail below).

Importantly, in many cases the round, mostly porous, grains are mantled by compact rims forming texturally composite grains (Fig. 6G, H). The compact rims represent overgrowths—a feature that is widespread in Jacobina. Round compact cores are also common but more difficult to be distinguished from the rims. Normally they can be recognized by etching and/or EMPA and LA-ICPMS geochemistry (to be discussed below). Secondary pyrite occurs predominantly as overgrowth and subordinately as newly crystallized euhedral grains (Fig. 6I) and vein fillings. Despite the challenges of accurately quantifying the proportions between the different pyrites, the secondary pyrite is perceived as the predominant type. Caution is advised with euhedral crystals as they can be the result of round detrital grains with cubic-terminated overgrowth. Thus, we recognize the following morphological pyrite types in Jacobina: round porous and round compact, both primary in origin, and the secondary overgrowth, euhedral crystals, and vein fillings. This preliminary morphological classification provides the fundamentals that, together with distinct chemical compositions, support the genetic classification proposed below.

Nickelian pyrite and siegenite (confirmed by EMPA) were identified as rims on compact round pyrite (Figs. 6J and 7B). Nickelian pyrite is also present as colloform clusters associated with goethite (Fig. 7C). In both cases, these associations occur near mafic dikes. Galena was identified as inclusions in round compact pyrite grains and intergrown with uraninite. Chalcopyrite occurs mostly associated with chalcocite and/or bornite, either free in the matrix of the metaconglomerates or as overgrowth on pyrite grains (Fig. 6K). Pyrrhotite and pentlandite were identified as 5–20 µm small inclusions in round compact pyrite with or without native gold (Figs. 6E, 8G and H).

Oxides and hydroxides

Hematite and goethite are abundant in Jacobina. They are the dominant accessory minerals in the oxidized ore assemblage but rare in the sulfide ore assemblage. Other oxides include rutile, uraninite, chromite, spinel, brannerite, and ilmenorutile. Hematite shows different habits, including blades, needles, and microcrystals. Randomly oriented hematite blades, up to 3 mm in length, were recorded in the LU Reef (Fig. 7A and B). Goethite occurs mostly as low-reflectance microcrystalline masses but also as blueish gray compact masses commonly marking the outline of cubic or round forms, presumably pyrite (Fig. 7C). Figure 5C illustrates the association between goethite and round particles of Chlorite 2.

Rutile occurs mostly as short compact euhedral to subhedral reddish-brown translucent crystals between 20 and 250 µm in length, either isolated or in clusters (Fig. 7D).

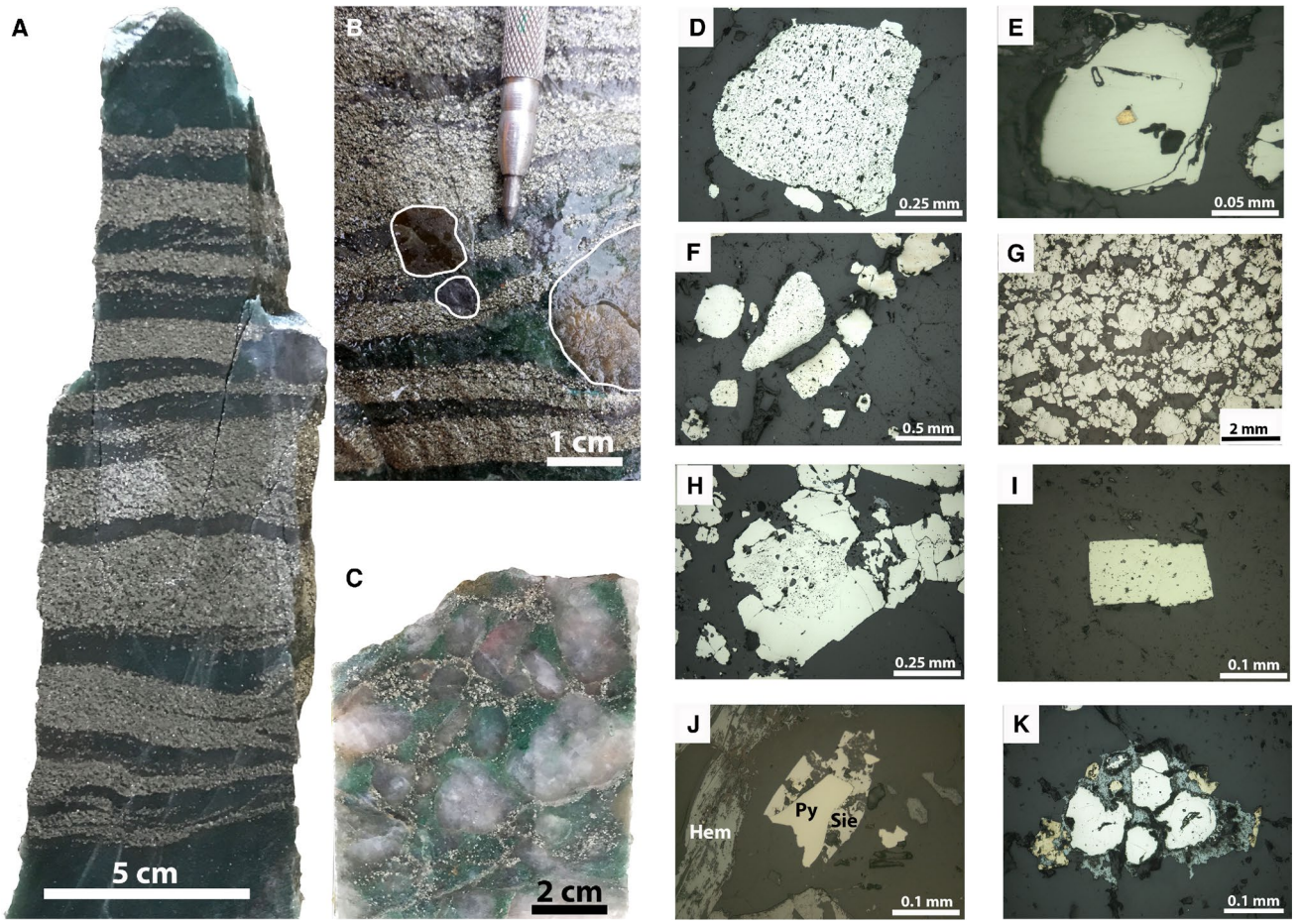

Fig. 6 Sulfides in hand specimens (**A**–**C**) and under reflected light (**D**–**K**). **A** Bedding-parallel pyrite layers (light colored) in dark green pebbly quartzite from the Holandês Reef sample JCBN21. **B** Detail of **A** showing pyrite grains conformably deposited in layers around quartz pebbles. **C** Pyrite (light-colored yellowish spots) in quartzitic matrix of a pebble- supported metaconglomerate of the LVLPC Reef sample JCBN33. **D** Porous round pyrite grain (white), fragmented on the right side, in quartzitic matrix (dark gray) sample JCBN50. **E** Compact round pyrite grain (yellowish white) with a central inclusion of gold and pyrrhotite in quartzitic matrix (dark gray) sample JCBN45. **F** Pyrite grains in a heavy mineral layer of the LVLPC Reef showing varied textures including round and angular grains with either porous and compact internal textures sample JCBN45. **G** Pyrite (yellowish white) in quarzitic matrix (dark gray), microscopic view of the hand specime exhibited in **A** and **B** sample JCBN21. **H** Pyrite (yellowish white) showing a large particle in the center of the image with round porous core and cubic-terminated compact rim in quartzitic matrix (dark gray) sample JCBN21. **I** Twinned euhedral pyrite cubes (yellowish white) in quartzitic matrix (dark gray) sample JCBN45. **J** Hematite (Hem) and pyrite (Py) surrounded by siegenite (Sie) in quartzitic matrix (darker gray) sample JCBN41. **K** Chalcopyrite and chalcocite (yellow and blueish gray, respectively) overgrowth on pyrite (white) grains in quartzitic matrix (dark gray) sample JCBN49

Locally, the clusters contain euhedral chromite grains in the same size range (Fig. 7E). Few isolated larger rutile grains are distinct from other rutile by having chromite inclusions and round outlines (Fig. 7F); these are interpreted as detrital grains. In places, rutile forms rims around ilmenorutile (Fig. 7G and H). Spinel was identified as a cluster of fine-grained (5–15 µm) euhedral to subhedral grains.

Uraninite is present as round grains predominantly associated with detrital pyrite in heavy mineral layers (Fig. 7I and J). Most of the uraninite grains contain pyrite inclusions or intergrowths. Also, tiny round fragments of pure uraninite were identified by EMPA in the matrix of the metaconglomerates (Fig. 7K). Like pyrite and rutile, the round uraninite grains are interpreted as detrital particles, analogous to those in the Witwatersrand (Depiné et al. 2013; Frimmel et al. 2014 and references therein). Rare irregularly shaped brannerite was identified in the same heavy-mineral layers and most likely represents an alteration product of uraninite (Fig. 7L).

Gold

Gold occurs in various morphological forms and mineral associations. A total of 154 gold grains were noticed under the microscope and grouped according to their morphology and texture. The majority of these (109 grains) correspond to free gold particles interstitial in the matrix of the metaconglomerates, whereas 33 are associated with fractures and veins, and 12 represent inclusions in detrital pyrite or quartz. The majority of the free gold particles shows irregular outlines (Fig. 8A), and a smaller fraction is circular or elliptical with smoothly rounded outlines (Fig. 8B and C). Analogously to the round detrital minerals described above, the round gold grains are tentatively interpreted as detrital. In this category, we include grains that are only slightly rounded (e.g., largest grain in Fig. 8D). Gold particles located in post-sedimentary structures, on the other hand, provide unequivocal evidence of Au transport by post-depositional fluids (Fig. 8E). The round gold particles are ≤ 70 µm in diameter, whereas irregular particles and structurally related, post-depositional hydrothermal gold attains larger dimensions. For instance, gold associated with shear planes reaches a few centimeters in length (Fig. 8F).

Gold was found in contact with the following minerals: quartz, pyrite, chlorite, rutile, goethite, and hematite. The association with quartz is the commonest as most of the gold is free in the quartzitic matrix (Fig. 8A–F), but gold was identified also as inclusions in a quartz pebble (to be described in more detail below). Gold within pyrite is present either as inclusions, together with other sulfide inclusions (Fig. 8G and H), or as vein fillings (Fig. 8I). Locally, gold appears intergrown with rutile and within chlorite cleavage planes (Fig. 8J). When associated with Fe-oxides and -hydroxides, gold occurs either intergrown or as inclusions (Fig. 8K and L).

The paragenetic sequence

Three main paragenetic stages can be distinguished in the metaconglomerates (ESM Table 7). Stage 1 involved the transport and deposition of detrital quartz and heavy minerals, including pyrite, zircon, rutile, uraninite, chromite, magnetite, spinel, galena, tourmaline, magnetite, molybdenite, thorite, ilmenorutile, and gold, which were concentrated in river channels. Stage 1 was followed by diagenesis, during which some chemical exchange was initiated, including partial pyrite remobilization. Naturally, primary minerals responded to post-depositional alteration according to their individual properties. Highly refractory zircon and ilmenorutile, for instance, are well preserved and restricted to Stage 1. Minerals formed at Stage 2 as a result of metamorphism and/or hydrothermal alteration include quartz, pyrite, rutile, gold, and newly formed phases, including muscovite/fuchsite, tourmaline, and brannerite. Stage 3 minerals formed during retrograde metamorphism, locally associated with late intrusions, include chlorite, pyrophyllite, hematite, goethite, and gold. Various secondary sulfides were generated during Stage 3, including bornite, chalcopyrite, covellite, chalcocite, linnaeite, sphalerite, digenite, and mackinawite.

Mineral chemistry, geothermometry, and metamorphism

Chlorite

A total of 84 microprobe spot analyses were carried out on chlorite grains distributed in four gold-mineralized samples: JCBN8 and JCBN31 from the Holandês Reef, and JCBN36 and JCBN41 from the LU Reef (ESM Table 2). The samples comprise quartz pebble metaconglomerates with variable proportions of chlorite, muscovite, hematite, goethite, pyrite, and rutile. Sample JCBN8 is a typical sulfide ore with pyrite as the dominant opaque phase, whereas Fe-oxides predominate in the other three samples. Samples JCBN8, JCBN31, and JCBN36 contain muscovite, whereas chlorite is the only phyllosilicate in sample JCBN41. Following

Fig. 7 Oxides and associated minerals in transmitted light **A**, **D**, ▸ and **G**, reflected light **B**, **C**, **E**, **F**, **H**, **I**, and **L**, and in backscattered images **J** and **K**. **A** Randomly oriented hematite blades (black) overprinting quartz (colorless) and chlorite (olive green) sample JCBN41. **B** Hematite blades (blueish gray), quartz (dark gray), chlorite (high relief dark gray), pyrite (white), and siegenite (light purpleish gray around pyrite); white rectangles indicate the position of zoomed-in images in Fig. 7J and 8L sample JCBN41. **C** Compact and microcrystalline goethite (blueish gray and darker gray, respectively), colloform nickelian pyrite (light-collored areas indicated as Ni-pyrite) in quartzitic matrix (gray); note that compact goethite forms roughly rectangular/cubic forms from presumably pyrite sample JCBN20. **D** Rutile crystals (reddish-brow), pyrite (black) in quartzitic matrix (colorless) sample JCBN44. **E** Rutile crystals (gray), pyrite (pale yellow), chromite (dark gray) in quartzitc matrix (darker gray) sample JCBN44. **F** Round rutile grain (greay) with chromite inclusions (darker gray) and pyrite (pale yellow) in quartzitic matrix (darkest gray) sample JCBN44. **G** Ilmenorutile grain (black, center of the image) with rutile rim (reddish-brown) in heavy mineral layer containing pyrite (black), quartz (white), and zircon (high relief third to fourth order interference color) sample JCBN5. **H** Same view as **G**, note the porous ilmenorutile grain surrounded by compact rutile sample JCBN5. **I** Round uraninite grain (gray) with several inclusions and surronded by a thin layer of pyrite (light gray) flanked by compact pyrite grains in quartzitic matrix (darker gray) sample JCBN45. **J** Round uraninite-pyrite grain sample JCBN44. **K** Round uraninite grain sample JCBN6. **L** Irregular brannerite-pyrite particle (center) sample JCBN45

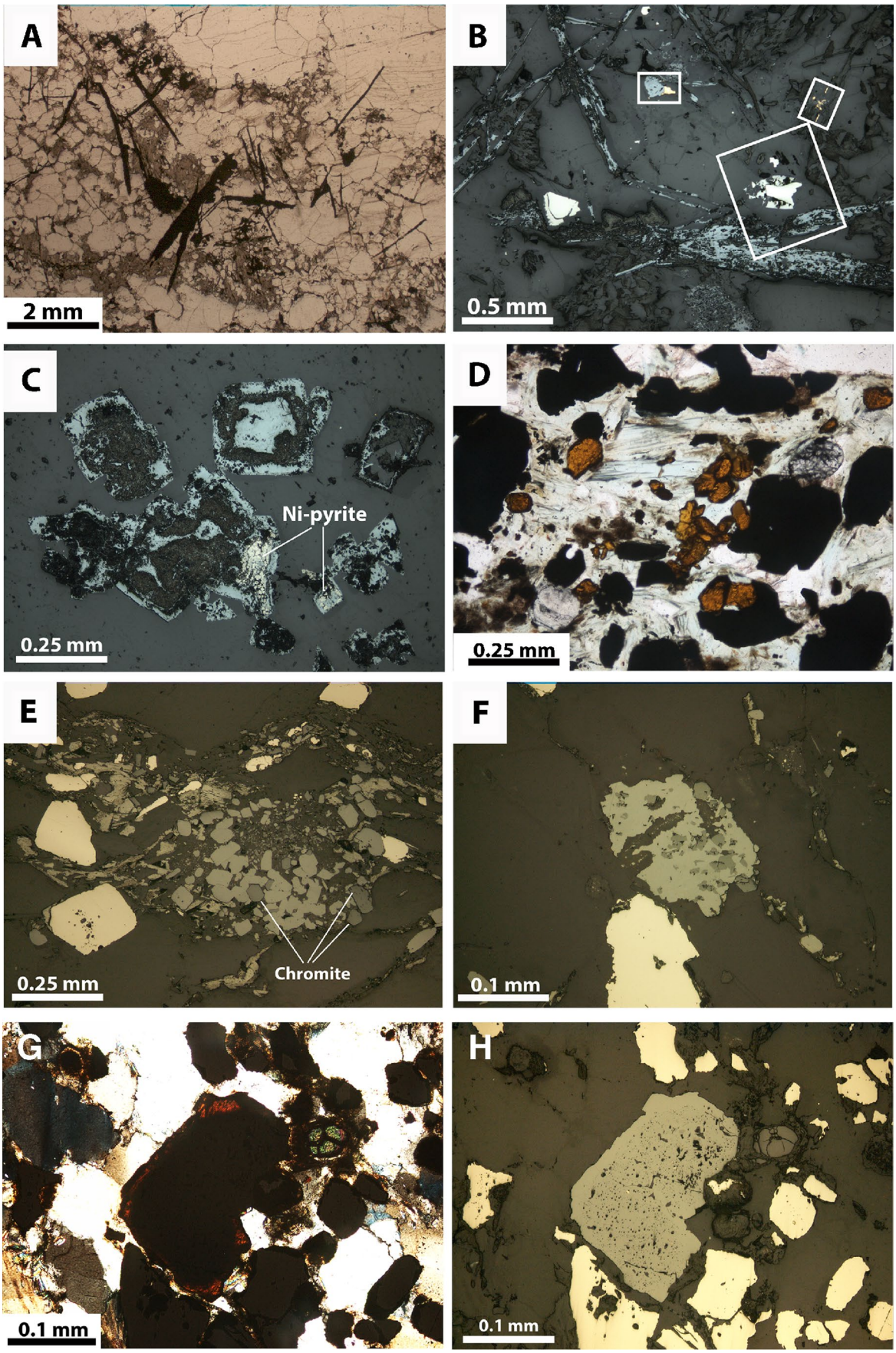
A
2 mm
B
0.5 mm
C
Ni-pyrite
0.25 mm
D
0.25 mm
E
Chromite
0.25 mm
F
0.1 mm
G
0.1 mm
H
0.1 mm

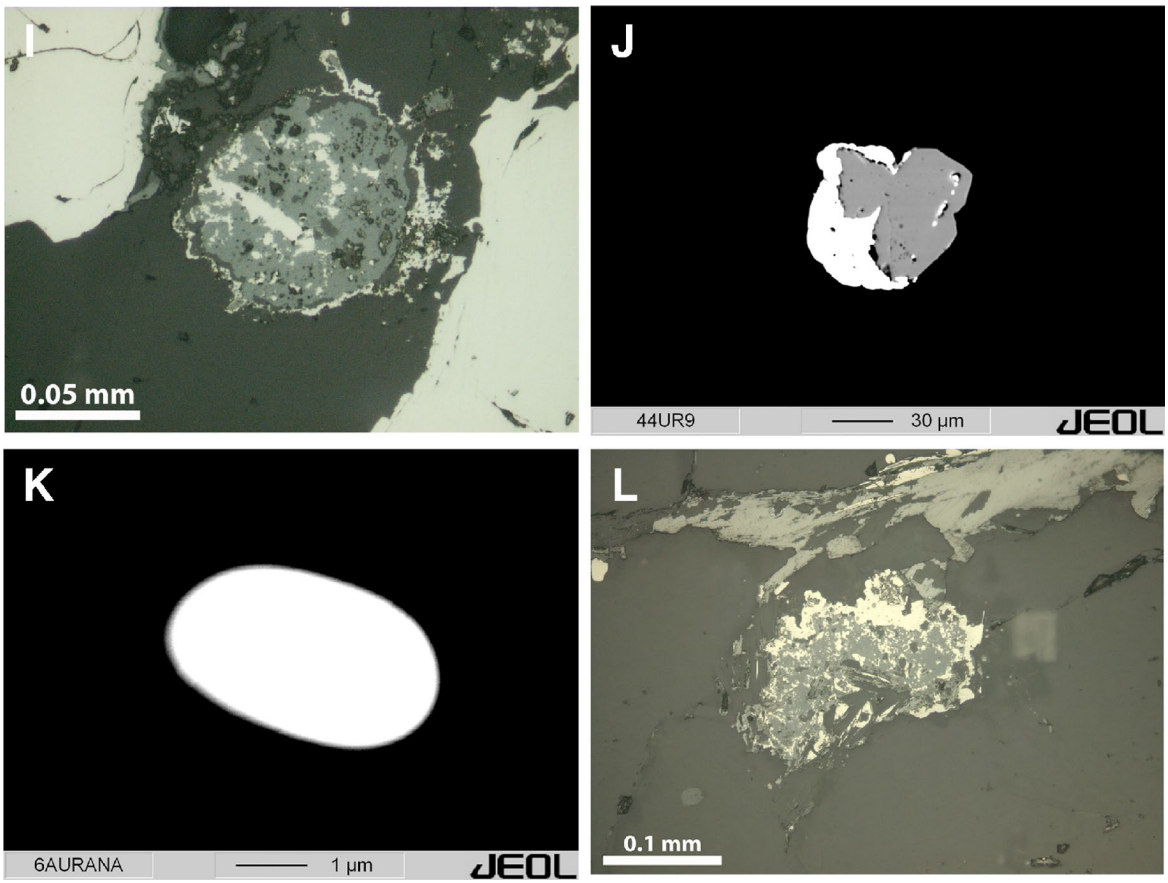

Fig. 7 (continued)

the classification proposed by Zane and Weiss (1998), the results indicate two distinct chemical compositions: Mg-chlorite (clinochlore, average Fe/(Fe + Mg) = 0.17) in samples JCBN8, JCBN36, and JCBN41, and Fe-chlorite (chamosite, average Fe/(Fe + Mg) = 0.91) in sample JCBN31 (ESM Fig. 1A). The chemically distinct Mg-chlorite and Fe-chlorite correspond to the textural types described above, i.e., Chlorite 1 and Chlorite 2, respectively. The dominant Mg-chlorite is disseminated in the matrix of the metaconglomerates with metamorphic quartz, muscovite, pyrite, and rutile (Fig. 5A and B). The round aggregates of Fe-chlorite with ± goethite, on the other hand, resemble pseudomorphs of possibly garnet or detrital ilmenite (Fig. 5 C).

The results of chlorite thermometry are summarized in ESM Fig. 1B. The analyses aimed at pure chlorite particles, avoiding areas of interlayering with other phyllosilicates and/or inclusions that could interfere with the Al contents. Analyses with detectable Ca, Na, and/or K were discarded as an extra precaution. Aluminum saturation was verified by the presence of muscovite in samples JCBN8, JCBN31, and JCBN36, except for sample JCBN41. Among the Mg-chlorite analyses, those in samples JCBN8 and JCBN36 yielded the narrowest temperature ranges, and a good consistency between different thermometers, whereas sample JCBN41 diverged from the trend with a wider temperature range that probably reflects some Al deficiency. Consequently, results from the samples JCBN8 and JCBN36 should best approximate the formation temperature of Mg-chlorite, i.e.,

Fig. 8 Gold in various forms and associations in reflected light in **A**, **E**, **G**–**L**, backscattered images in **B**, **C**, and **D**, and macrophotograph (**F**). **A** Irregular gold particles (yellow) in quartzitic matrix (dark gray) sample JCBN38. **B**, **C**, and **D** Round gold grains (white) in quartzitic matrix (black) sample JCBN6, note that the central grain in **D** has a roughly rectangular outline with round corners. **E** Gold (yellow) filling veinlet in quartz pebble (dark gray), note darker linear areas marking fluid inclusion tracks internal to the pebble sample JCBN17 . **F** Gold on shear plane in hand specimen sample JCBN17. **G** and **H** Gold (yellow), pyrrhotite (brown), and galena (blueish gray) inclusions in pyrite (white) in quarzitic matrix (black) sample JCBN32. **I** Gold (yellow) filling quartz-pyrite (dark gray and pale yellow, respectively) vein sample JCBN16. **J** Gold (yellow), rutile (blueish gray), and chlorite (high relief dark gray) in quartzitic matrix (dark gray) sample JCBN41. **K** Gold (yellow) in contact with microcrystalline goethite (dark brownish gray, higher relief) in quartzitic matrix (dark brownish gray, lower relief) sample JCBN26. **L** Hematite (blueish gray), gold (yellow) in quartzitic matrix (black) sample JCBN41. Note tiny gold inclusions in hematite

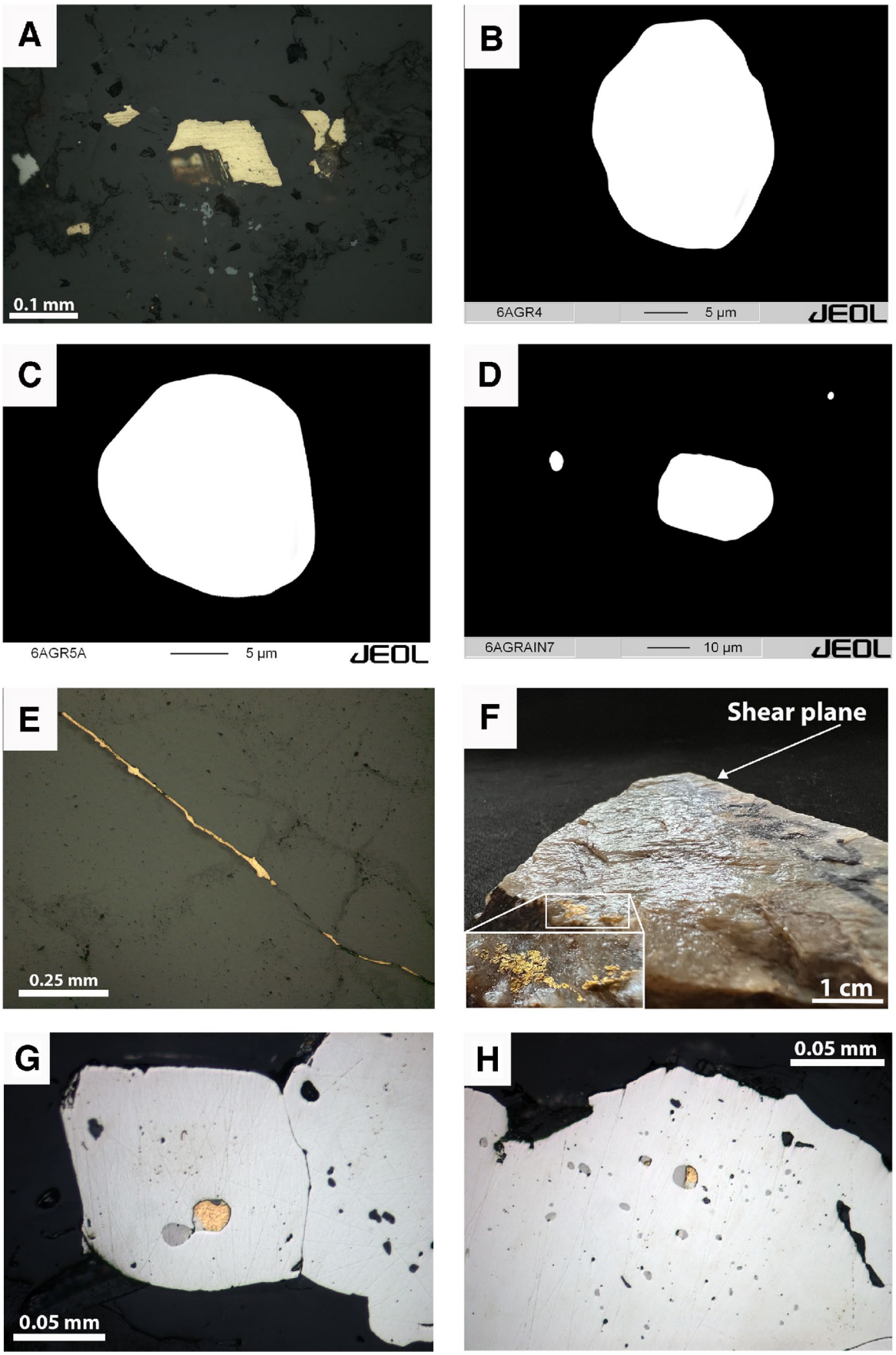
A
0.1 mm
B
6AGR4
5 µm
JEOL
C
6AGR5A
5 µm
JEOL
D
6AGRAIN7
10 µm
JEOL
E
0.25 mm
F
Shear plane
1 cm
G
0.05 mm
H
0.05 mm

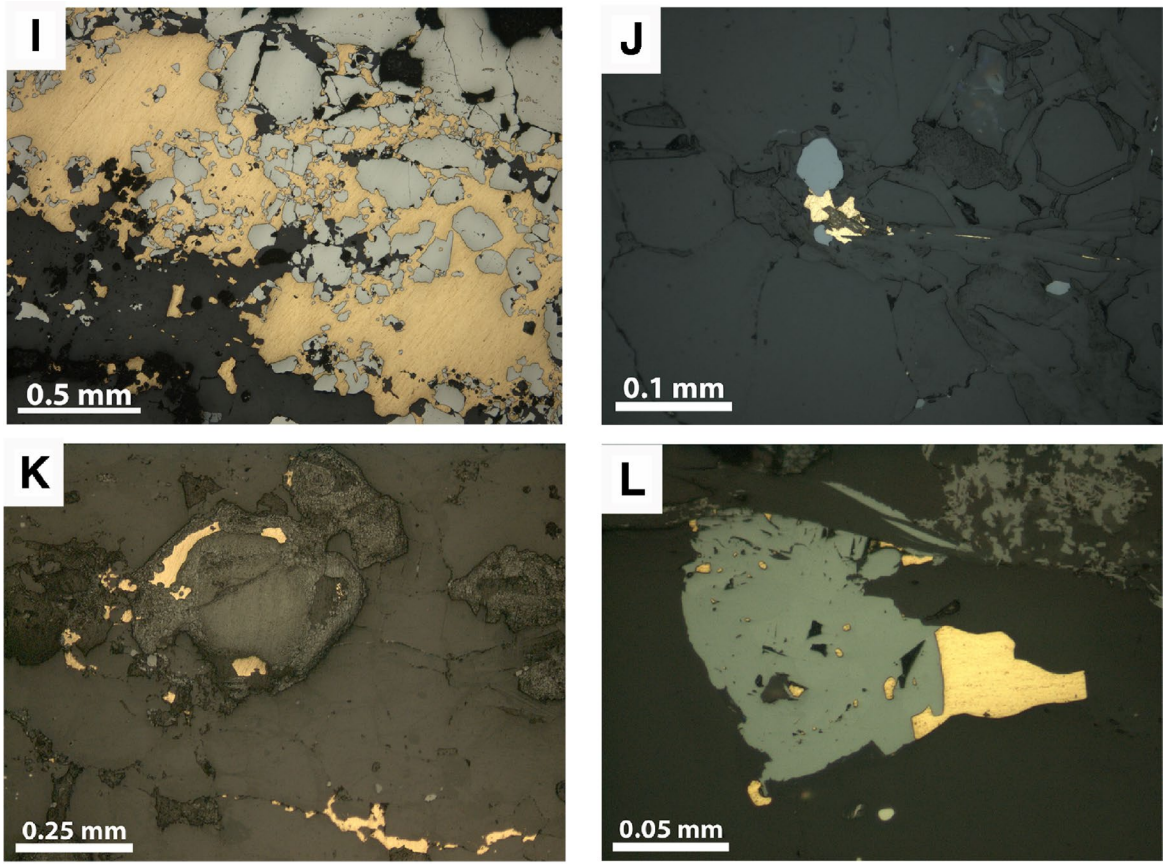

Fig. 8 (continued)

289–339 °C. For the Fe-chlorite analyses in sample JCBN31, only Zang and Fyfe's and El-Sharkawy's thermometers were used because Fe/(Fe + Mg) correction is not considered in Cathelineau and Nieva (1985). The temperatures calculated are between 277 and 317 °C and thus within the error of those for the Mg-chlorite above. Similar Fe-chlorite was described by Miranda et al. (2021) in gold-bearing major thrust faults that cut through the Jacobina Group. Both sets of Fe-chlorite correspond to chamosite (ESM Fig. 1A). We agree with the above authors, that the Fe-chlorite formed during retrograde metamorphism associated with the final stages of the Paleoproterozoic Orogeny, when the Jacobina Group rocks were uplifted to higher crustal levels. The Mg-chlorite is regarded as coeval with the Fe-chlorite and formed under similar conditions in which case the difference in composition probably reflects only very local chemical equilibration on a mineral grain scale and thus a low fluid/rock ratio.

Tourmaline

The chemical composition of tourmaline was determined on 58 spots in 41 tourmaline grains in three gold-mineralized samples: JCBN2 (MSPC Reef), JCBN17 (Basal Reef), and JCBN38 (MU Reef) (ESM Table 3). Larger grains were tested for internal chemical zonation and no significant heterogeneity was observed. The tourmaline occurs as optically homogeneous euhedral to subhedral crystals with no indication of sedimentary abrasion. According to the classification proposed by Henry et al. (2011), the composition of the tourmaline is predominantly dravitic, with Mg/(Mg + Fe) between 0.33 and 1, total Al between 5.14 and 6.00 atoms per formula unit, and anomalously high Cr concentrations between 1.04 and 9.83 wt% Cr_2O_3 (ESM Fig. 2). Fluorine concentrations are notably low. These characteristics suggest that the tourmaline is metamorphic in origin. The majority of the analyses spread within the fields of Cr-, V-, and Al-rich metasedimentary rocks on the Al–Mg-Fe diagrams of Henry and Dutrow (2018) (ESM Fig. 3). A few analyses from sample JCBN38 fall into the field of Li-poor granitic rocks, but these represent a minor proportion in a sample with predominant metamorphic affiliation. Milesi et al. (2002) suggested that detrital and hydrothermal tourmalines in Jacobina could be distinguished based on the Cr contents, but no two distinct populations can be recognized within that wide data range.

Pyrite

A total of 93 LA-ICPMS analyses (ESM Table 4A) was conducted on the three distinct morphological types of pyrite in samples JCBN8 (Holandês Reef), JCBN11 (FW Main Reef), and JCBN14 (Main Reef). From the 18 elements analyzed, nine were detected in most of the analyses: As, Co, and Ni, detected at levels of hundreds of ppm; Pb at that of tens of ppm; and Ag, Au, Cu, Cd, and Tl, detected in single digit ppm concentrations. The other nine elements (Hg, Ir, Mo, Os, Pd, Pt, Re, Rh, and Ru) were detected in less than nine spots. Table 1 presents the average trace element contents for each of the three morphological pyrite types. With respect to the more common trace elements, the compact round pyrite recorded the highest average Ni content, whereas the porous round pyrite has the highest As and the secondary pyrite the highest Co contents. A relatively lower Co/Ni ratio, on average 1.1, distinguishes the secondary pyrite from both the round compact and the round porous pyrite, both with Co/Ni ratios of, on average, 1.9. Notably, the round porous pyrite shows a good correlation between Co and Ni (correlation coefficient = 0.75) compared to the round compact pyrite (correlation coefficient = 0.52) and secondary pyrite (correlation coefficient = 0.23). Also noteworthy is colloform nickelian pyrite with up to 18.8 wt% Ni identified within goethite in an oxidized ore sample (Fig. 7C).

The most significant compositional differences between the three morphological pyrite types are related to Pb, Cu, Au, and Ag. The round porous pyrite has the highest contents of these elements, whereas the secondary pyrite is notably depleted in all of them (Table 1). The difference is most pronounced in Au content, which differs by one order of magnitude between the pyrite types, with the round porous pyrite having the highest Au content. Noteworthy is the relatively low Au/Ag ratio of secondary pyrite (= 1) compared to the other two types (round porous pyrite: 4, round compact pyrite: 2). Also of note is the good correlation between Cu, Au, Ag, and Cd in secondary pyrite (ESM Table 4B). The contrast in trace element contents is most evident in texturally composite pyrite grains. Figure 9 illustrates the situation, in which natural oxidization of the polished surface of thin sections reveals the chemical contrast between different pyrite generations. The rounded porous cores returned higher concentrations of Au, Cu, and Ag than their respective compact rims (Fig. 9A and B). The round compact cores also exhibit contrasting composition in relation to their respective rims (Fig. 9C), but the trace element contents in the compact cores can be lower than in the rims, as illustrated in the pyrite grain of Fig. 9D that shows higher Au and Ag but lower Cu contents.

Table 1 Trace element contents of different pyrite types as obtained by LA-ICPMS

		As (ppm)	Co (ppm)	Ni (ppm)	Pb (ppm)	Cu (ppm)	Au (ppm)	Ag (ppm)	Tl (ppm)	Cd (ppm)	Au/Ag
Round compact pyrite (detrital)	Mean	202	363	404	7.17	1.70	0.22	0.11	1.09	0.21	2
	Range	30.7–703	25.1–1,38	46.9–1,35	1.80–15.50	< 0.20–4.73	0.11–0.39	< 0.02–0.22	< 0.01–3.86	< 0.07–0.37	
Round porous pyrite (synsedimentary)	Mean	833	446	277	41.0	3.21	1.34	0.33	0.09	0.14	4
	Range	32.5–9,180	74.7–1,654	40.7–787	1.86–158	< 0.20–11.4	0.07–10.9	0.03–1.82	< 0.01–0.68	< 0.07–0.23	
Secondary compact pyrite	Mean	320	519	298	2.30	0.68	0.04	0.04	0.11	0.20	1
	Range	0.61–1,121	1.84–1,240	8.53–1,352	< 0.01–53.3	< 0.15–9.00	< 0.01–0.08	< 0.01–0.26	< 0.01–2.90	< 0.01–0.50	

Rutile

A total of 94 EMP analyses (ESM Table 5) was conducted on 36 rutile grains within four gold-mineralized samples: JCBN5 (LU Reef), JCBN22 (LMPC Reef), JCBN26 (FW Main Reef), and JCBN44 (MSPC Reef). The most conspicuous trace elements detected were Cr and Nb, with contents between 0.80–2.76 wt% Cr_2O_3 and 0.36–1.38 wt% Nb_2O_5. A rutile rim around an ilmenorutile grain has even higher contents of Cr and Nb (3.76 wt% Cr_2O_3 and 3.10 wt% Nb_2O_5). The ilmenorutile grain contains 58.2–60.5 wt% TiO_2, 19.9–22.7 wt% Nb_2O_5, and 3.43–3.74 wt% FeO, and Ta determined qualitatively. The analyses also revealed Al_2O_3 contents between 1.08 and 1.22 wt% and MgO contents of 0.21 to 0.23 wt%, which probably reflect minute inclusions of other minerals.

Milesi et al. (2002) distinguished two types of rutile in Jacobina based on texture, Cr content, and U–Pb age. According to these authors, the first type consists of large, black, low-Cr, rounded grains, which they interpreted as detrital, and the second type comprises red, translucent, euhedral to subhedral crystals with high Cr contents, interpreted as post-depositional hydrothermal in origin. Based on the U–Pb geochronological work conducted by Mougeot (1996), they report "a clear Archean heritage" for the detrital rutile and a Proterozoic (≈ 2.04 Ga) age for the red hydrothermal rutile.

The characteristics of the red rutile (Fig. 7D and E) match the description of the red rutile of Milesi et al. (2002). It probably formed through dissolution and reprecipitation during the Paleoproterozoic Orogeny, analogously to some of the rutile described in the Moeda Formation (another metaconglomerate-hosted gold deposit located some 1000 km to the south of Jacobina) by Zeh et al. (2018). Detrital rutile and ilmenite are the most likely sources of Ti for the red rutile. The ilmenorutile depicted in Fig. 7G is probably also detrital and experienced post-depositional alteration while serving as a substrate for the epitaxial overgrowth of red rutile. Notably, the Jacobina red rutile contains the highest Cr and Nb contents compared to other studies on rutile composition, including other metaconglomerate-hosted gold deposits (ESM Fig. 4 and references therein).

The results of the Zr-in-rutile thermometry are presented as histograms in ESM Fig. 5. Interestingly, the histograms reflect the improved precision and perhaps higher accuracy achieved with the progressive development of the method. Thus, Zack et al.'s (2004a) thermometer resulted in a wider temperature range between 646 and 810 °C, followed by Watson et al. (2006) with a range from 598 to 704 °C. Tomkins et al.'s (2007) thermometer was calculated for pressures of 3 kb and 4 kb, based on estimates proposed previously (Ledru et al. 1997; Milesi et al. 2002; Leite et al. 2007), and yielded 577–678 °C for 3 kb and 582–683 °C for 4 kb. The calibration by Tomkins et al. (2007) is regarded as the most reliable (Zack and Kooijman 2017), so the modal interval of 600–650 °C is taken as the best estimate for the rutile formation temperature in the Jacobina metaconglomerates. Also noteworthy is the negligible difference between the results obtained for 3 kb and 4 kb using the Tomkins et al. (2007) thermometer. Although the rutile temperatures calculated here surpass, on average, the 600 °C peak metamorphic temperature suggested by metapelitic phase equilibria, the difference is statistically not significant because the temperatures derived from both methods overlap. The calculated Zr-in-rutile temperatures probably approximate peak metamorphic conditions thus confirming the metamorphic nature of the red rutile generation.

Gold

A total of 351 microprobe analyses was conducted on 154 gold particles (ESM Table 6). Gold, Ag, and Cu were detected whereas Hg and Pd were below the lower limit of detection of 0.05 wt%. Gold concentrations are between 92.3 and 100.6 wt%, whereas Ag and Cu attain maxima of 6.62 wt% and 0.57 wt%, respectively (Table 2). The results indicate an average composition of the Jacobina gold as 98.3 wt% Au, 1.54 wt% Ag, and 0.07 wt% Cu. The Ag content in the Jacobina gold exhibits a polymodal distribution with major modes in the intervals 0.6–0.9, 1.9–2.2, and minor ones at 3.2–3.5 and 6.0–6.3 wt% Ag (ESM Fig. 6A). In contrast, the Cu content shows a skewed distribution with the main mode in the interval 0.03–0.05 wt% Cu, a second mode in 0.27–0.30 wt% Cu, and a couple of outliers at 0.51 and 0.57 wt% Cu (ESM Fig. 6B).

Most of the gold exhibits homogeneous composition within a given sample. However, there are a few exceptions in which gold can be distinguished based on both morphology and Ag content. For instance, a frequency distribution diagram from the Basal Reef and the FW Main Reef shows outliers with highly pure gold composition (ESM Fig. 6C). In the Basal Reef, the high-fineness gold occurs as veinlets that crosscut fluid inclusion trails containing tiny gold inclusions with Ag contents above 2.59 wt% (Fig. 10B and C). These inclusions returned up to 5.19 wt% Ag, but unfortunately, due to the very small size of the analyzed spots, they returned low totals. In this

Fig. 9 Microphotographs of round porous pyrite (**A** and **B**) and round compact pyrite (**C** and **D**) surrounded by compact overgrowth with anhedral to euhedral terminations. Dark spots of approximately 40 µm in diameter mark laser ablation pits from ICPMS analysis, Au, Cu, and Ag results. Note different colors created by natural oxidation of the polished surface of the thin sections. The colors reflect different pyrite generations

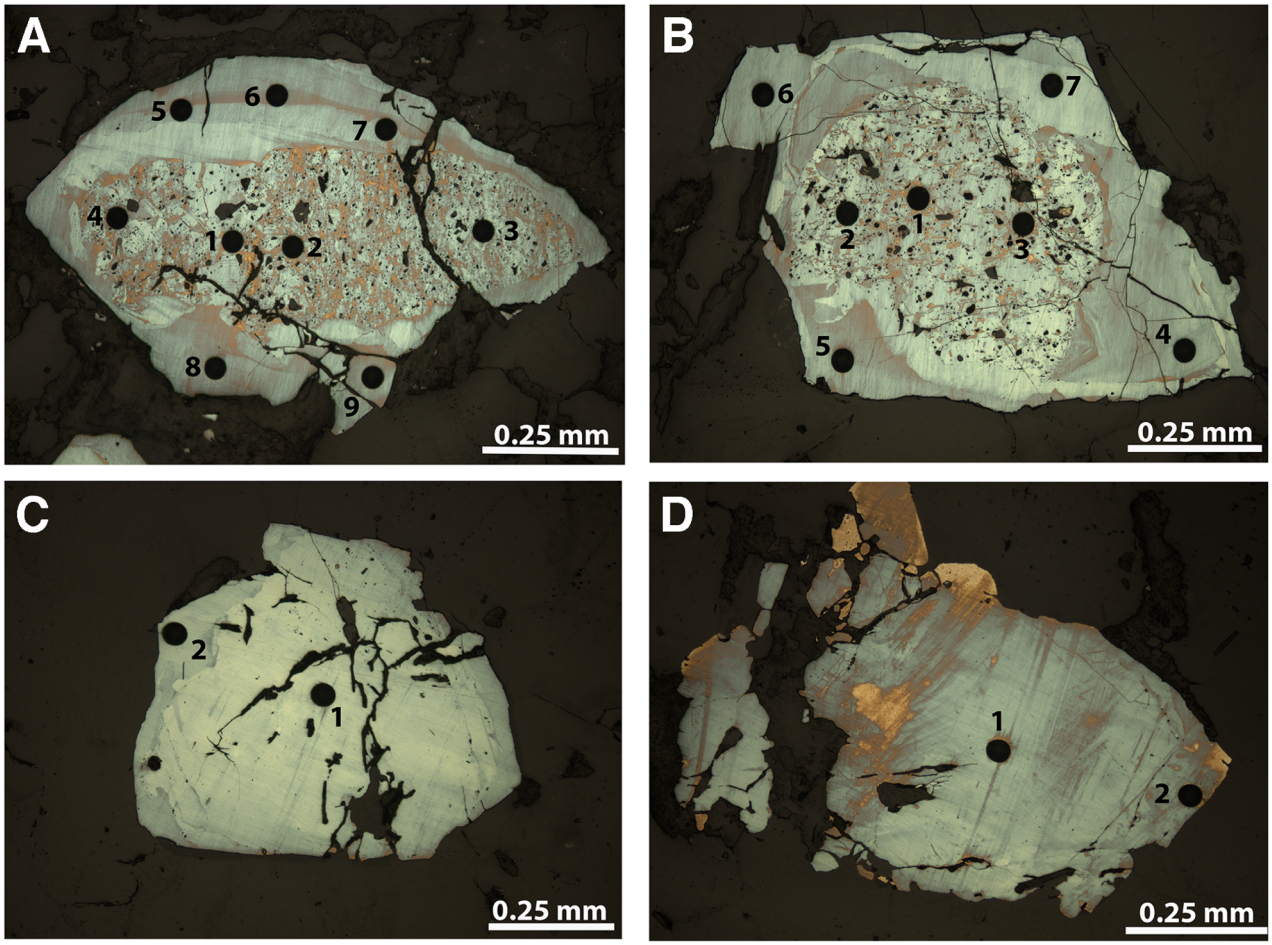

Grain	Pyrite type	Spot	Au (ppm)	Cu (ppm)	Ag (ppm)
A	Porous core	1	0.249	4.27	0.203
		2	0.366	3.52	0.290
		3	0.935	3.38	0.311
		4	0.529	5.13	0.232
	Compact Rim	5	0.067	<0.224	<0.014
		6	<0.011	<0.213	<0.012
		7	0.024	<0.230	<0.012
		8	<0.014	<0.218	<0.015
		9	<0.014	<0.211	0.124
B	Porous core	1	0.205	1.33	0.118
		2	0.446	1.37	0.122
		3	0.302	1.96	0.130
	Compact Rim	4	0.012	<0.170	<0.012
		5	<0.013	<0.169	<0.013
		6	<0.009	<0.158	<0.007
		7	0.028	<0.158	<0.007
C	Round Comp. Core	1	0.193	4.73	0.161
	Compact Rim	2	0.082	0.309	<0.011
D	Round Comp. Core	1	0.287	<0.247	0.031
	Compact Rim	2	0.079	0.928	0.024

Table 2 Jacobina gold composition

	Average (wt%)	Minimum (wt%)	Maximum (wt%)
Au	98.3	92.3	100.6
Ag	1.54	BD	6.62
Cu	0.07	BD	0.57

BD, below detection

context, we recognize two gold generations: the first is allogenic and is represented by the Ag-bearing gold inclusions, and the second is characterized by the high-fineness gold remobilized in veinlets, thus indicating a refining effect of post-depositional gold remobilization (compare Fig. 10B and C with D and E). In the FW Main Reef, the temporal relationship is not self-evident, but the high-fineness gold occurs as isolated particles among remobilized gold with Ag content of around 2 wt%. In both examples, purification of gold by remobilization is evident. Another exception is the variation in Ag content between round gold grains from the MSPC reef. These homogenous grains have the following average Ag contents per particle: 1.13 wt%, 1.95 wt%, 1.99 wt%, 2.09 wt%, 5.56 wt%, 6.19 wt%, and 6.62 wt%. This is a wide range compared to other samples, and considering the probable detrital nature of the grains, their distinct composition might reflect variable provenance.

Although most of the gold particles are internally homogenous, some compositional heterogeneity was observed in round gold grains from the Liberino Reef. In this case, the analyses indicate different Ag concentrations between the center and the edge of a grain (3.48 wt% Ag at the center against 0.52 wt% and 0.11 wt% Ag at the edges). Microprobe elemental maps obtained from the two grains in that sample revealed Ag-depleted rims on both grains (ESM Fig. 7). Such a feature might be misinterpreted as Ag-depleted rim as typically observed in recent gold placers (Groen et al. 1990; Putnis 2009). However, the reducing conditions of the Archean atmosphere under which these grains were deposited would not support this interpretation. Instead, the Ag-depleted rims are regarded as post-depositional hypogene alteration, which must have had an overall effect on the Ag content of the Jacobina gold. The rims show, however, that the alteration process may have been locally peripheral, and some of the original composition remained preserved in the core of the gold grains.

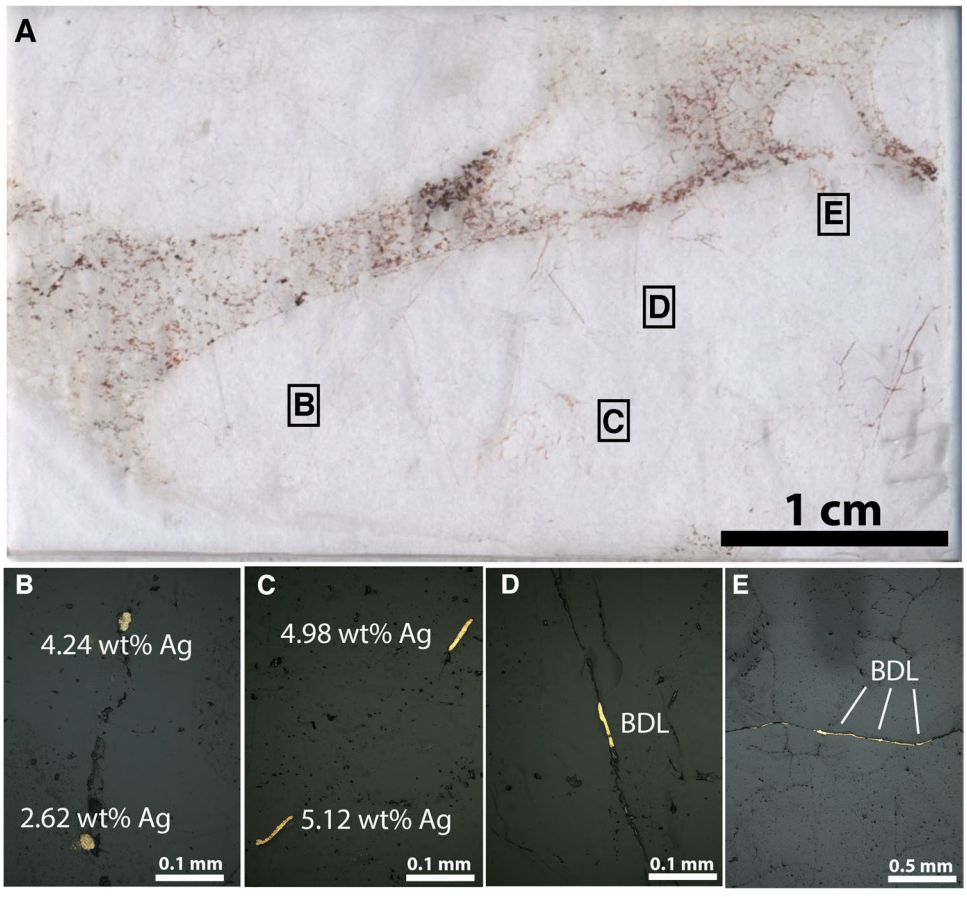

Fig. 10 Gold inclusions and veinlets in quartz pebble of the Basal reef. **A** Thin section image showing the location of microphotographs. **B** Round gold inclusions along fluid inclusion track. **C** Elongated gold inclusions along fluid inclusion track. **D** Gold filling microfracture. **E** Gold veinlet crosscutting fluid inclusion tracks (zoom in detail in Fig. 9E). Numbers refer to Ag contents by EMPA. BDL = below detection limit. Numbers represent the average of 2 spot analyses on each gold particle. Analyses on **B** (top) and **C** returned low totals (< 98%) due to the reduced size of the inclusion, and were not considered in the statistics, but are displayed here to illustrate the differences in Ag contents between two gold generations

The Jacobina gold mineralization

Allogenic mineralization

Quartz and pyrite are the dominant minerals in the Jacobina ore assemblage. Whereas well-rounded quartz pebbles and sands provide convincing textural evidence of their detrital nature, pyrite displays a wide variety of textures that indicate more complex and diverse origins. Hendrickson (1984), in a first attempt to classify the different types of pyrite in Jacobina, identified rounded grains and interpreted them as detrital particles. This iconic pyrite is the predominant type in the Witwatersrand (Hallbauer 1986) where it has been regarded by almost all earlier workers as detrital (Ramdohr 1955; Saager 1969; Utter 1978; Hallbauer 1986; Minter et al. 1988; MacLean and Fleet 1989). Although challenged by supporters of the various hydrothermal models (Phillips and Myers 1989; Barnicoat et al. 1997; Phillips and Law 2000), the notion of this pyrite type being detrital has been consolidated throughout the years with the support of petrography, trace element data, and isotope geochemistry (England et al. 2002; Hofmann et al. 2009; Koglin et al. 2010; Guy et al. 2014; Agangi et al. 2015). Genetically of great significance at Jacobina is the observation that gold inclusions can be found in both detrital pyrite and detrital quartz (Figs. 6E, 8G and H, and 10B and C). This provides additional evidence that gold was carried into the depositional basin with the sediment load and thus represents the first gold mineralizing stage in Jacobina.

Gold-mineralized source rocks and their mechanically transported fragments are expected to release gold into the watercourses. This process has been described in modern placers (Knight et al. 1994; Youngson and Craw 1999; and references therein) as well as in the Witwatersrand (Hallbauer and Utter 1977; Utter 1979, 1980; Minter et al. 1993; Frimmel 2014). Due to softness and malleability of the gold, abrasion and hammering during transport result in rounding and flattening of the gold particles. Minter et al. (1993) estimated that more than 75% of a population of over 5000 gold grains from a given sample of Witwatersrand ore had rounded forms to which they attributed a detrital origin—a finding that has been since then corroborated by in-situ analyses of the gold morphology by µ-XRD-CT (Frimmel 2018). They also pointed out that detrital grains can have knobby surfaces as a result of peening caused by the sediment abrasion. Hendrickson (1984) pioneered the identification of detrital gold in Jacobina. In the present study we identified 22 round gold grains that strongly support his observations (e.g., Fig. 8B, C, and D). Furthermore, the knobby outlines of round gold grains identified here (ESM Fig. 7) can be ascribed to sediment abrasion as suggested by Minter et al. (1993) for the Witwatersrand gold.

Placer gold composition may reflect the compositional variability of its provenance (von Gehlen 1983; Frimmel and Gartz 1997). Despite the post-depositional alteration at Jacobina, distinct differences exist in gold composition that suggests a provenance control. The internally homogeneous and compositionally distinct gold grains from the MSPC Reef described above suggest a provenance-related compositional signature. This may also be the case for the distinct gold composition identified between the main stratigraphic units. This is apparent in Ag versus Cu diagrams (ESM Fig. 8), from the base, the FW Main Reef gold (Lower Conglomerate unit) clusters around 2 wt% Ag; the gold from the Lu, Mu, and LVLPC reefs (Upper Conglomerate–Lower Unit) clusters around 1 wt% Ag; and the Piritoso, Liberino, and Holandês reefs (Upper Conglomerate–Intermediate Unit) contain gold with around 3 wt% Ag. Interestingly, a couple of analyses from the Piritoso Reef (Upper Unit) coincide with the Lower Conglomerate Unit suggesting that gold from the lower units may have been mechanically recycled into younger metaconglomerates. The Ag-depleted rims of the gold grains from the Holandês Reef (ESM Fig. 7) indicate that Ag depletion may not have been complete on a grain-scale. Thus, the overall Ag contents seemingly became decreased by post-depositional fluids, but locally, some of the primary differences in Ag content can still be discerned.

The second gold mineralization process recognized in the metaconglomerate-hosted gold deposits is associated with another type of pyrite, described here as porous round pyrite. This pyrite type is considered synsedimentary. Such a genetic interpretation is endorsed by petrography, trace element geochemistry, and isotope data (e.g., Hallbauer 1986; England et al. 2002; Hofmann et al. 2009; Koglin et al. 2010; Guy et al. 2014; Agangi et al. 2013, 2015 and references therein). The atmospheric and hydrospheric conditions that prevailed during the Mesoarchean, including extremely low atmospheric O_2 and elevated CO_2, CH_4, SO_2, and H_2S concentrations, enabled significant quantities of Au and other metals to be dissolved in rivers and subsequently captured by early microbes to form the first major concentration of gold in Earth's history (Frimmel 2005, 2014, 2018; Frimmel and Hennigh 2015; Heinrich 2015).

Synsedimentary pyrite is part of the Jacobina ore assemblage. Figure 6D displays a grain with a typical porous internal texture that, although fragmented on the right side, still shows a well-rounded contour indicating abrasion during sediment transport. Figure 6F illustrates a typical heavy mineral layer with grains and angular fragments of porous synsedimentary and round compact pyrite grains. One particular feature of the synsedimentary pyrite in Jacobina is that it displays a more restricted textural diversity than in the Witwatersrand. The specimens identified in the present

study resemble the mud-ball pyrite of Hallbauer (1986) or the detrital aggregates of England et al. (2002). This does not necessarily indicate the absence of specific types, but probably reflects the fact that most of these fragile structures were not resistant enough to endure abrasion during transport.

We have shown in the present study that, like in other metaconglomerate-hosted gold deposits (Koglin et al. 2010; Ulrich et al. 2011; Large et al. 2013; Agangi et al. 2013, 2015), the synsedimentary pyrite is characterized by elevated trace element contents (Table 1, Fig. 9A and B), a feature that supports the findings of Teles et al. (2020), who named the synsedimentary type inclusion-bearing pyrite, following the nomenclature proposed by da Costa et al. (2017). Our data show that the average Au content in the synsedimentary pyrite is two orders of magnitude higher than that of the secondary pyrite (Table 1). The synsedimentary pyrite, therefore, represents a genetically distinct pyrite generation, and based on its consistently elevated Au contents, provides evidence of a syngenetic gold mineralization stage in Jacobina, typical of the richest Witwatersrand-type paleoplacer gold deposits in South Africa.

Post-depositional mineralization

Abundant secondary pyrite and other metamorphic/hydrothermal minerals like chlorite, fuchsite, rutile, tourmaline, and Fe-oxides/hydroxides are the most evident indicators of post-depositional alteration in Jacobina. The process through which the secondary pyrite formed is not fully established. Teles et al. (2020) suggested that the detrital pyrite recrystallized during metamorphism to form the epigenetic pyrite. This is debatable. Pyrite was certainly remobilized, as evident from textures and the compositional differences described in the previous sections. However, typical high-grade metamorphic textures, such as annealing, triple junctions, or the presence of porphyroblasts/granoblasts, which would clearly indicate pyrite recrystallization (Craig and Vokes 1993, and references therein), have not been observed at Jacobina. Moreover, peak metamorphic temperatures of ca. 600 °C, as determined by phase equilibria and Zr-in-rutile thermometry, indicate that temperatures just reached the pyrite recrystallization threshold (Cox et al. 1981), but have not exceeded the pyrite thermal stability, which according to Craig et al. (1998) extends to ca. 740 °C at low pressure. Under these conditions, some local recrystallization might be possible, but certainly not extensive or prevalent. Furthermore, the primary textures and contrasting compositions between pyrite types indicate that pyrite overgrowth, which according to McClay and Ellis (1983) is typical of lower metamorphic conditions, took place all along the prograde path of metamorphism. Alternatively, a fluid-mediated process involving partial dissolution and reprecipitation, as proposed for the Witwatersrand (Frimmel 1994), offers a more plausible explanation for the remobilization of pyrite and its trace elements in Jacobina. Therefore, the lower Au/Ag ratio of the post-depositional pyrite suggests that Au was decoupled from Ag during pyrite remobilization. Also, the very good correlation between Cu, Au, and Ag in the post-depositional pyrite (ESM Table 4B) indicates a cognate relationship between these elements. Thus, it is suggested that pyrite was remobilized, and Au within the pyrite was released during this process in Jacobina. The very poor correlation between Pb and Au, on the other hand, suggests that Pb was controlled by a different source, probably radiogenic Pb derived from decaying detrital uraninite.

Approximately 20% of the gold occurrences observed in the present study are associated with microstructures like veinlets, microfractures, and mineral cleavage. As such, they provide textural evidence of gold mobilization/remobilization as exemplified by gold infilling a quartz-pyrite vein, which is oblique to the bedding and confined to the boundaries of the Holandês Reef (Fig. 8I). Notably, this gold generation occupies a late paragenetic position in relation to secondary quartz and pyrite. In another example described above, pure gold fills microfractures in a gold-mineralized quartz pebble, showing two distinct gold generations side by side (Fig. 10). Additional examples of gold remobilization are gold particles in shear planes (Fig. 8F), gold infilling chlorite cleavage (Fig. 8J), and gold intergrown with Fe-oxides (Fig. 8L). All primary forms of gold, namely, allogenic gold in detrital pyrite, gold incorporated in synsedimentary pyrite, and detrital gold particles represent potential sources for gold remobilization. Gold in veins that cut through the Jacobina Group, studied by Miranda et al. (2021), most likely reflects the same stage of retrograde fluid infiltration at temperatures between about 300 and 350 °C.

The extent of the gold remobilization is variable and difficult to quantify. In the case of the Holandês Reef discussed in the previous paragraph, where the vein is confined to the reef, the immediate surrounding rock is the most probable source of the vein material. In this case, Au must have traveled within the meter-thick metaconglomerate (internal remobilization). In contrast, there are situations where gold was mobilized with hematite into fractures and microfractures for > 100 m into the barren footwall or hanging wall quartzites (external remobilization). In other cases, the alteration is found near mafic intrusions, suggesting that at least some of these occurrences are related to magmatism—probably a result of heat-driven fluid convection through the host rock (Fig. 8L). In these cases of external remobilization, the alteration surpassed the reef limits causing a dispersion effect on gold and consequently producing small uneconomic

gold concentrations in the vicinity of the main orebodies. Gold remobilization in Jacobina was certainly more extensive than in the Witwatersrand, where it was mainly internal within the metaconglomerates (Frimmel et al. 1993; Frimmel 1994).

As described above, remobilization at Jacobina clearly led to a change in gold composition with Ag-depletion by post-depositional fluids. Compared with other metaconglomerate-hosted gold deposits, the Jacobina gold has a unique composition characterized by the following: (a) relatively low Ag content, (b) presence of Cu in low concentrations, and (c) absence of Hg. The Witwatersrand gold has been reported in several studies to contain far higher Ag and Hg contents between 0.3–32.1wt% and 0.5–5.9 wt%, respectively, and traces of the following elements: As, Bi, Cd, Co, Cr, Cu, Fe, Ir, Mn, Mo, Ni, Os, Pb, Pd, Pt, Re, Ru, Se, Sb, Sn, Ta, Te, and V (Saager 1969; Feather and Koen 1975; Hallbauer and Utter 1977; Utter 1979; von Gehlen 1983; Hallbauer 1986; Oberthür and Saager 1986; Reid et al. 1988; Minter et al. 1990; Garayp et al. 1991; Frimmel et al. 1993; Frimmel and Gartz 1997).

The presence of Cu in most of the gold analyses also sets the Jacobina gold apart, because in other metaconglomerate-hosted gold deposits Cu occurs only in trace amounts and has been attributed mostly to mineral inclusions (Frimmel et al. 1993; Frimmel and Gartz 1997). The EMPA elemental maps referred to above show Cu homogeneously distributed across the entire grains, suggesting that the metal is alloyed with gold (ESM Fig. 7). Also, analyses of externally remobilized gold feature as outliers in Cu-in-gold histograms with the highest Cu contents (ESM Fig. 6B), suggesting that gold may have been enriched in Cu during the most advanced stages of remobilization.

Regarding the lack of Hg in the Jacobina gold, it cannot be precluded that the detrital gold particles there initially contained some Hg. The much higher temperatures attained during peak metamorphism (ca. 600 °C) would be sufficient to destabilize the system Au–Ag-Hg and release Hg into the metamorphic fluid. Hallbauer (1986) tested the phenomenon through an experiment in which he heated alloyed Au–Ag-Hg particles in a closed microscope stage and monitored the release of Hg. The conclusion reached was that Hg is released at temperatures between 350 and 420 °C. Thus, the absence of Hg in the Jacobina gold is expected to be a result of metamorphism.

An important aspect of the mineralization history is oxidation, mainly because hematite and goethite appear locally associated with gold. Genetically relevant are the following observations: (i) hematite crystals overprint the metamorphic fabric (Fig. 7A and B) at places close to a mafic intrusive body, (ii) oxidation affected both primary and secondary pyrite, leading to the formation of either hematite or goethite (Figs. 7C, 8L), (iii) the analyzed samples come from > 600 m below surface, which precludes recent weathering as cause of the oxidation, and (iv) oxidation is widespread, but not pervasive, to a point where locally Fe-oxides/hydroxides just permeate the sulfide ore. Consequently, oxidation is clearly late in the paragenetic sequence. Pearson et al. (2005) associated the oxidation to late oxidizing fluids related to the emplacement of post-tectonic mafic to intermediate dikes. The hematite blades in Fig. 7A and B resemble thermal metamorphic textures. There is consensus that the mafic and ultramafic intrusive bodies became metamorphosed (Molinari and Scarpelli 1988; Teixeira et al. 2001; Milesi et al. 2002; Pearson et al. 2005) and the rock associated with the hematite blades is a quartz-clinochlore schist, interpreted as a metamorphosed mafic intrusive. Thus, at least some of the oxidation may have been caused by the intrusion of hot basic to ultrabasic melts, triggering convective flow of meteoric waters. This took place during uplift in the final stages of the Paleoproterozoic Orogeny, long after the Great Oxidation Event. This is supported by observations by Miranda et al. (2021) who found evidence of fluid mixing due to a decrease in pressure during uplift. Importantly, the widespread oxidation must have contributed to the Ag-depletion enabling Ag-poor gold to precipitate. Thus, in the absence of direct radiometric age control, we tentatively ascribe the oxidation to Stage 3.

Genetic model

After the discussions on the Jacobina metallogeny in the 1950s (White 1956; Bateman 1958; Davidson 1957), the controversy seemed conciliated by the modified paleoplacer model (Cox 1967; Gross 1968), until the early 2000s when Teixeira et al. (2001) proposed an epigenetic model for the Jacobina gold mineralization. Soon thereafter, Milesi et al. (2002) attempted to combine a "shear-zone-related epigenetic mineralization" with the paleoplacer concept into what they named hydrothermal shear-reservoir model. However, none of the works placed much emphasis on the paleoplacer model. Since then, Teixeira et al. (2010, 2019) have reiterated their epigenetic model and advocated against the paleoplacer model based on the argument that the thickness of the mineralized zone (290 m considering the upper and the lower metaconglomerates) would be excessive for a placer deposit. As described above, the thick mineralized zone actually combines a series of individual centimeter- to meter-thick placer increments. Note that, in comparison, the gold-rich Central Rand Group in South Africa attains an overall thickness of as much as 2.9 km.

The Jacobina gold mineralization is the result of a complex sequence of processes that started with the concentration of gold in placers, with strong lithological and sedimentological control on gold grade as well as the presence of rounded gold particles and gold inclusions within detrital quartz and pyrite providing perhaps the strongest argument for this. Some subeconomic concentrations of gold also occur in finer grained siliciclastic units, probably related to some Au dispersion by post-depositional fluids, but the metaconglomerates are the principal host of the gold, as evident in the spatial distribution of Au grade across stratigraphic levels depicted in Fig. 11. This feature is characteristic not only of the locality for which the figure was drawn but of the entire ore district.

The regional metamorphism and magmatism associated with the Paleoproterozoic Orogeny caused, without doubt, significant post-depositional alteration of the Jacobina gold deposits and their host rocks. Thrust and wrench tectonics affected the whole succession and formed the framework and physico-chemical conditions for remobilization of gold and pyrite. The detrital pyrite and gold that had been already present in the conglomerates provided the most likely source of the secondary pyrite and gold, respectively. Fluids flowing along faults and magmas intruding into the succession certainly incorporated gold from the already existing placer deposits. There are indications of magmatic fluids in the system (Milesi et al. 2002; Teles et al. 2020; Miranda et al. 2021; and this study), and it is expected that the early mafic/ultramafic intrusives and the late to post-tectonic granites influenced the post-depositional alteration, however only on a very local scale within tens of meters. For instance, the hematite blades overprinting metamorphic fabric are spatially restricted to a continuous 50-m alteration zone in the vicinity of a mafic intrusive in the LU Reef (Fig. 7A and B). In this case, the host rock is a gold-mineralized metaconglomerate, in which gold was reprecipitated together with Fe-oxides/hydroxides. As the intrusive rock was derived from a H_2O-deficient magma, the fluids involved were most likely not magmatogenic but meteoric, circulating through the host rocks by thermal convection. In the case of the granites, the influence of the magmatic fluids is also local. For instance, only very few analyses indicate a magmatic affiliation of some tourmaline in a sample in wich most of the tourmaline is otherwise metamorphic (ESM Fig. 3). Only local magmatic influence is also suggested by the fluid inclusion study of Miranda et al. (2021), who found vapor-rich H_2O-NaCl fluids of allegedly magmatic derivation only in the Mina Velha deposit, out of four deposits studied. Whether the magmatic fluids provided any new gold to the system remains uncertain but even if it did, this had little influence on the overall gold endowment of the metaconglomerates.

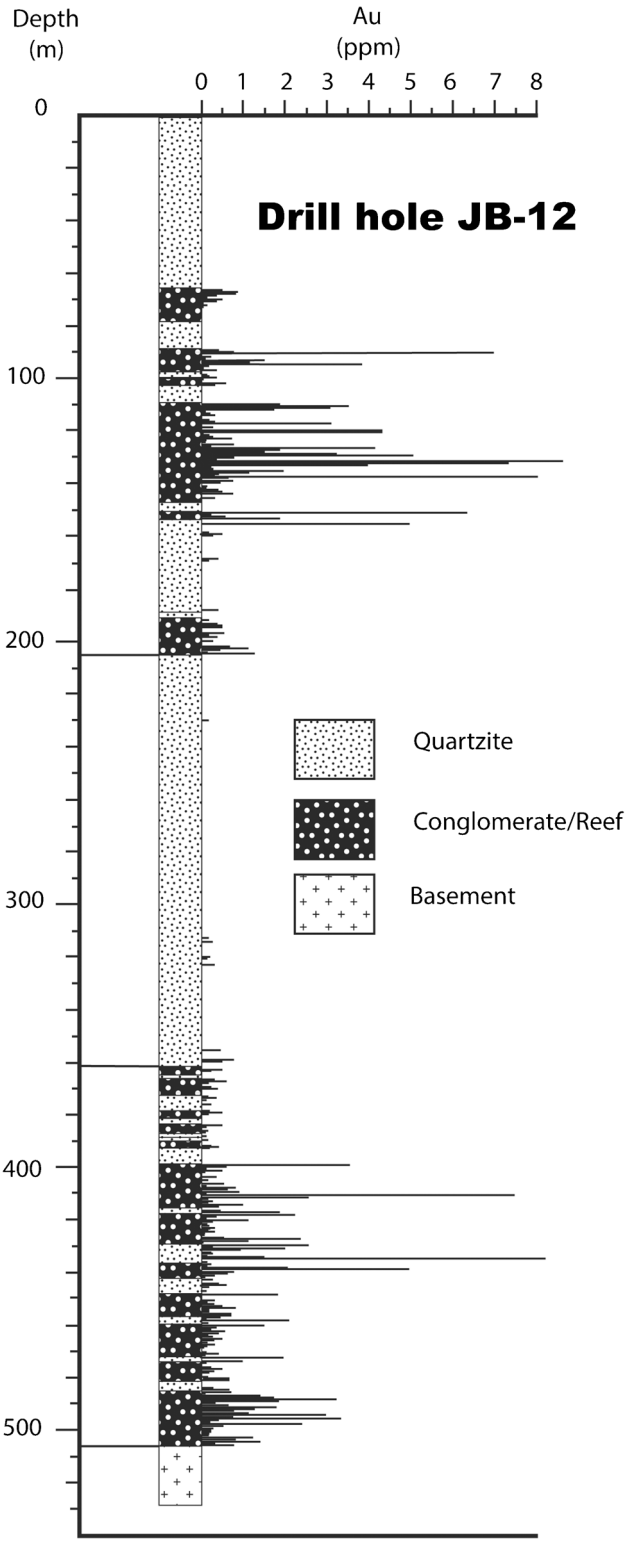

Fig. 11 Schematic diagram modified from Teixeira et al. (2001) showing the gold distribution along drillhole JB-12 in the João Belo Mine. The gold dispersion pattern shows a strong correlation between conglomeratic units and Au grade

Conclusions

There is substantial evidence of primarily placer gold concentration at Jacobina, that is, strong lithological and sedimentological control on Au grade at different scales, presence of detrital minerals with gold inclusions within heavy mineral layers, and of detrital gold particles.

Three genetic types of pyrite were recognized: detrital, synsedimentary, and post-depositional pyrite. These can be correlated to the pyrite types identified in the Witwatersrand Basin and other examples of metaconglomerate-hosted gold deposits. Widespread pyrite overgrowth masks the primary pyrite, which can lead to overestimation of the proportion of secondary pyrite. Each pyrite type had a particular role to play in the gold mineralization process: whereas the detrital and the synsedimentary types accompanied gold accumulation in the placer, the post-depositional pyrite resulted from a fluid-induced remobilization event that led to Au depletion in primary pyrite.

The presence of synsedimentary pyrite with significantly higher Au concentrations in relation to the other pyrite types supports elevated Au contents, probably dissolved as Au-sulfide complex, in surface waters at the time as suggested by Frimmel (2014), Frimmel and Hennigh (2015), and Heinrich (2015). The proportion and textural diversity of the synsedimentary pyrite in Jacobina are comparatively low, which may be the result of mechanical abrasion during sediment transport, selectively obliterating more fragile mineral structures.

What distinguishes the Jacobina deposits from other Witwatersrand-type gold deposits is the nature and extent of post-depositional alteration, mainly in the course of the Paleoproterozoic Orogeny. Phase equilibria and application of Zr-in-rutile thermometry suggest peak metamorphic temperatures of ca. 600 °C. Metamorphism and magmatism caused the partial dissolution and reprecipitation of various minerals including pyrite and gold. This remobilization of both pyrite and gold changed their trace element contents, thus resulting in gold of greater fineness. Compared with other Witwatersrand-type gold deposits, Jacobina gold composition is characterized by relatively low Ag contents, the presence of Cu at low concentrations, and the absence of Hg, all of which can be ascribed to fluid-induced remobilization at elevated temperatures. Despite the purifying effect of the post-depositional alteration, some gold particles still maintain some compositional distinction between the main stratigraphic units that may reflect a provenance-related signature.

There is indication of local magmatic influence on the gold mineralization history. Mafic/ultramafic intrusives caused a thermal overprint, whereas late- to post-tectonic granite emplacement triggered hydrothermal fluid circulation and further partial remobilization of ore components. The latter took place under very different redox conditions, evident from the presence of Fe-oxides/hydroxides associated with remobilized gold. This suggests some gold remobilization after the Great Oxidation Event, which is in agreement with the age of the late to post-tectonic magmatism (1970 to 1800 Ma). In summary, based on the evidence of placer gold concentration and the intense post-depositional alteration, the modified paleoplacer model best fits the Jacobina gold deposits.

Supplementary Information The online version contains supplementary material available at https://doi.org/10.1007/s00126-023-01220-9.

Acknowledgements S. Höhn, U Schüßler, and N. Koglin assisted with microprobe analyses, and H. Brätz and R. Klemd are thanked for respectively conducting and enabling the LA-ICPMS analyses. We also thank Yamana Gold Inc. for providing access and logistic support to their operations in Jacobina. The analytical costs were covered by the Department of Geodynamics and Geomaterials Research at the University of Würzburg. Comments by D. Miranda, and two anonymous reviewers as well as the associate editor, A. Cabral, and editor, B. Lehmann, helped to improve the original manuscript.

Funding Open Access funding enabled and organized by Projekt DEAL.

Declarations

Competing interests The authors declare no competing interests.

References

Agangi A, Hofmann A, Wohlgemuth-Ueberwasser CC (2013) Pyrite zoning as a record of mineralization in the Ventersdorp Contact Reef, Witwatersrand Basin, South Africa. Econ Geol 108:1243–1272

Agangi A, Hofmann A, Rollion-Bard C, Marin-Carbonne J, Cavalazzi B, Large R, Meffre S (2015) Gold accumulation in the Archaean Witwatersrand Basin, South Africa – evidence from concentrically laminated pyrite. Earth-Sci Rev 140:27–53

Almeida FFM (1977) O cráton do São Francisco. Revista Brasileira De Geociências 7:349–364

Almeida FFM (1981) O cráton do Paramirim e suas relações com o do São Francisco. Simpósio Sobre o Cráton do São Francisco e Suas Faixas Marginais Salvador 1981 SBG-Núcleo Bahia Salvador Anais pp 1–10

Barbosa JSF, Sabaté P (2004) Archean and Paleoproterozoic crust of the São Francisco Craton, Bahia, Brazil. Precamb Res 133:1–27
Barnicoat AC, Henderson IHC et al (1997) Hydrothermal gold mineralization in the Witwatersrand basin. Nature 386:820–824
Bateman JD (1958) Uranium-bearing auriferous reef at Jacobina, Brazil. Econ Geol 53:417–425
Cathelineau M, Nieva D (1985) A chlorite solid solution geothermometer The Los Azufres (Mexico) geothermal system. Contrib Mineral Petrol 91:235–244
Cathelineau M (1988) Cation site occupancy in chlorites and illites as a function of temperature. Clay Miner 23:471–485
Couto PA et al. (1978) Projeto Serra de Jacobina: geologia e prospecção geoquímica. Relatório Final. Vol.1 Companhia de Pesquisa de Recursos Minerais, Superintendência de Salvador, Convênio CPRM-DNPM, Salvador, Brasil pp 415
Cox DP (1967) Regional environment of the Jacobina auriferous conglomerate, Brazil. Econ Geol 62:773–780
Cox SF, Etheridge MA, Hobbs BE (1981) The experimental ductile deformation of polycrystalline and single crystal pyrite. Econ Geol 76:2105–2117
Craig JR, Vokes FM (1993) The metamorphism of pyrite and pyritic ores: an overview. Miner Mag 57:3–18
Craig JR, Vokes FM, Solberg TN (1998) Pyrite: physical and chemical textures. Miner Deposita 34:82–101
Da Costa G, Hofmann A, Agangi A, (2017) Provenance of detrital pyrite in Archaean sedimentary rocks: examples from the Witwatersrand Basin. In: Mazumder R, (ed) Sediment Provenance – influences on compositional change from source to sink. Elsevier pp 509–531
Davidson CF (1957) On the occurrence of uranium in ancient conglomerates. Econ Geol 52:668–693
De Caritat P, Hutcheon I, Walshe JL (1993) Chlorite geothermometry: a review. Clays Clay Minerals 41(2):219–239
Delgado IM et al (2003) Geotectônica dos escudos das Guianas e Brasil-Central In: Bizzi LA, Schobbenhaus C, Vidotti RM, Gonçalves JH (eds) Geologia, Tectônica e Recursos Minerais do Brasil. Serviço Geológico do Brasil CPRM, Brasília, Brasil pp 227–334
Depiné M, Frimmel HE, Emsbo P, Koenig AE (2013) Trace element distribution in uraninite from Mesoarchaean Witwatersrand conglomerates (South Africa) supports model and magmatogenic source. Miner Deposita 48:423–435
Dos Santos FP, Chemale Junior F, Meneses ARAS (2019) The nature of the Paleoproterozoic orogen in the Jacobina Range and adjacent areas, northern São Francisco Craton, Brazil, based on structural geology and gravimetric modeling. Precambr Res 332:1–20
El-Sharkawy MF (2000) Talc mineralization of ultramafic affinity in the Eastern Desert of Egypt. Miner Deposita 35:346–363
England GL, Rasmussen B, Krapez B, Groves D (2002) Paleoenvironmental significance of rounded pyrite in siliciclastic of the Late Archean Witwatersrand Basin: oxygen-deficient atmosphere or hydrothermal alteration? Sedimentology 49:1133–1156
Ewing TA, Hermann J, Rubatto D (2013) The robustness of the Zr-in-rutile and Ti-in-zircon thermometers during high-temperature metamorphism (Ivrea-Verbano Zone northern Italy). Contrib Miner Petrol 165:757–779
Farquhar J, Zerkle AL, Bekker A (2011) Geological constraints on the origin of oxygenic photosynthesis. Photosynthesis Res 10791:11–36
Feather CE, Koen GM (1975) The minerology of the Witwatersrand reefs. Minerals Sci Eng 7:189–224
Frimmel HE (1994) Metamorphism of the Witwatersrand gold. Explor Mining Geol 3:357–370
Frimmel HE (2005) Achaean atmospheric evolution: evidence from the Witwatersrand gold fields, South Africa. Earth-Sci Rev 70:1–46
Frimmel HE (2014) A giant Mesoarchean crustal gold-enrichment episode: possible causes and consequences for exploration. Soc Econ Geol Spec Publ 18:209–234
Frimmel HE (2018) Episodic concentration of gold to ore grade through Earth's history. Earth-Sci Rev 180:148–158
Frimmel HE, Le Roex AP, Knight J, Minter WEL (1993) A case study of the postdepositional alteration of the Witwatersrand Basal Reef gold placer. Econ Geol 88:249–265
Frimmel HE, Gartz VH (1997) Witwatersrand gold particle chemistry matches model of metamorphosed, hydrothermally altered placer deposits. Miner Deposita 32:523–530
Frimmel HE, Minter WEL (2002) Recent developments concerning the geological history and genesis of the Witwatersrand gold deposits, South Africa. Soc Econ Geol Spec Publ 9:17–45
Frimmel HE, Groves DI, Kirk J, Ruiz J, Chesley J, Minter WEL (2005) The formation and preservation of the Witwatersrand goldfields, the world's largest gold province. In: Hedenquist JW, Thompson JFH, Goldfarb RJ, Richards JP (eds) Economic Geology One Hundreth Anniversary Volume. Society of Economic Geologists, Littleton, pp 769–797
Frimmel HE, Schedel S, Brätz H (2014) Uraninite chemistry as forensic tool for provenance analysis. Appl Geochem 48:104–121
Frimmel HE, Hennigh Q (2015) First whiffs of atmospheric oxigen triggered onset of crustal gold cycle. Miner Deposita 50:5–26
Frimmel HE, Nwaila GT (2020) Geologic evidence of syngenetic gold in the Witwatersrand goldfields, South Africa. In: Sillitoe RH, Goldfarb RJ, Robert F, Simmons SF (eds) Geology of the World's Major Gold Deposits and Provinces. Soc Econ Geol Spec Publ 23: 645–668
Garayp E, Minter WEL, Renger FE, Siegers A (1991) Moeda placer gold deposits in the Ouro Fino Syncline, Quadrilátero Ferrífero, Brazil. In: Ladeira EA (ed) Brazil Gold '91 The Economics, Geology, Geochemistry and Genesis of Gold Deposits. A.A. Balkema, Rotterdam, pp 601–608
Groen JC, Craig JR, Rimstidt JD (1990) Gold-rich rim formation on electrum grains in placers. Can Mineral 28:207–228
Gross WH (1968) Evidence for a modified placer origin for auriferous conglomerates, Canavieiras Mine, Jacobina, Brazil. Econ Geol 63:271–276
Guy BM, Ono S, Gutzmer J, Beukes NJ (2014) Sulfur sources of sedimentary "buckshot" pyrite in the auriferous conglomerates of the Mesoarchean Witwatersrand and Ventersdorp supergroups, Kaapvaal Craton, South Africa. Miner Deposita 49:751–775
Hallbauer DK (1986) The mineralogy and geochemistry of Witwatersrand pyrite, gold, uranium, and carbonaceous matter. In: Anhaeusser CR, Maske S (eds) Mineral Deposits of Southern Africa. Geol Soc South Africa, Johannesburg, pp 731–752
Hallbauer DK, Utter T (1977) Geochemical and morphological characteristics of gold particles from recent river deposits and the fossil placers of the Witwatersrand. Miner Deposita 12:293–306
Heinrich CA (2015) Witwatersrand gold deposits formed by volcanic rain, anoxic rivers and Archean life. Nature Geosci 8:206–209
Hendrickson BR (1984) Stratigraphic position, mineralogy, depositional environment, and gold distribution of the Main Reef at Morro do Cuscuz and Morro do Vento near Jacobina, Bahia, Brazil. Unpubl MSc thesis, South Dakota School of Mines and Technology, Rapid City, USA
Henry DJ, Dutrow BL (2018) Tourmaline contributions through time: contributions to scientific advancements. J Geosci 63:77–98
Henry DJ, Novák M, Hawthorne FC et al (2011) Nomenclature of the tourmaline-supergroup minerals. Am Mineral 96:895–913
Hillier S, Velde B (1991) Octahedral occupancy and the chemical composition of diagenetic (low-temperature) chlorites. Clay Miner 26:149–168
Hofmann A, Bekker A, Rouxel O, Rumble D, Master S (2009) Multiple sulphur and iron isotope composition of detrital pyrite in the

Archean sedimentary rocks: a new tool for provenance analysis. Earth Planet Sci Lett 286:436–445
Holland HD (2006) The oxygenation of the atmosphere and oceans. Phil Transact R Soc B 361:903–915
Horscroft FDM, Mossman DJ, Reimer TO, Hennigh Q (2011) Witwatersrand metallogenesis: the case for (modified) syngenesis. SEPM Spec Publ 101:75–95
Inoue A, Inoué S, Utada M (2018) Application of chlorite thermometry to estimation of formation temperature and redox conditions. Clay Miner 53:143–158
Knight JB, Mortensen JK, Morison SR (1994) Shape and composition of lode and placer gold from the Klondike District Yukon, Canada. Bulletin 3 Exploration and Geological Services Division, Indian and Northern Affairs Canada pp 142
Koglin N, Frimmel HE, Minter WEL, Brätz H (2010) Trace-element characteristics of different pyrite types in Mesoarchaean to Palaeoproterozoic placer deposits. Miner Deposita 45:259–280
Kooijman E, Smit MA, Mezger K, Berndt J (2012) Trace element systematics in granulite facies rutile: implications for the Zr geothermometry and provenance studies. J Metamorphic Geol 30:397–412
Kranidiotis P, Maclean WH (1987) Systematics of chlorite alteration at the Phelps Dodge massive sulfide deposit, Matagami, Quebec. Econ Geol 82:1898–1911
Large RR, Meffre S, Burnett R, Guy B, Bull S, Gilbert S, Goemann K, Danyushevsky L (2013) Evidence for an intrabasinal source and multiple concentration in the formation of the Carbon Leader, Witwatersrand Supergroup, South Africa. Econ Geol 108:1215–1241
Ledru P, Johan V, Milesi JP, Tegyey M (1994) Markers of the last stages of the Paleoproterozoic collision for a 2 Ga continent involving circum-South Atlantic provinces. Precamb Res 69:169–191
Ledru P, Milesi JP, Johan V, Sabaté P, Maluski H (1997) Foreland basins and gold-bearing conglomerates: a new model of the Jacobina Basin (São Francisco province, Brazil). Precamb Res 86:155–176
Leite CMM, Barbosa JSF, Nicollet C, Sabaté P (2007) Evolução metamórfica/metassomática Paleoproterozóica do Complexo Saúde, da Bacia de Jacobina e de leucogranitos peraluminosos na parte norte do Cráton do São Francisco. Revista Brasileira De Geociências 37(4):777–797
Leo GN, Cox DP, Carvalho JPP (1964) Geologia da Parte Sul da Serra de Jacobina, Bahia, Brasil. DNPM Boletim 209 Rio de Janeiro pp 87
Luvizotto GL, Zack T (2009) Nb and Zr behavior in rutile during high-grade metamorphism and retrogression: an example from the Ivrea-Verbano Zone. Chem Geol 261:303–317
MacLean PJ, Fleet ME (1989) Detrital pyrite in the Witwatersrand Gold Fields of South Africa: evidence from truncated growth banding. Econ Geol 84:2008–2011
Mascarenhas JF, Conceição Filho VM, Griffon JC (1992) Contribuição à geologia do Grupo Jacobina, região Jacobina/Pindobaçu. Congresso Brasileiro De Geologia Boletim De Resumos Expandidos SBG Brasil 2:141–142
Mascarenhas JF, Silva EFA (1994) Greenstone Belt de Mundo Novo: caracterização e implicações metalogenéticas e geotectônicas no Cráton do São Francisco. Série Arquivos Abertos 5, Companhia Baiana de Pesquisa Mineral, Salvador pp 31
Mascarenhas JF, Ledru P, Souza SL, Conceição Filho VM, Melo LFA, Lorenzo CL, Milési JP (1998) Geologia e recursos minerais do Grupo Jacobina e da parte sul do Greenstone Belt de Mundo Novo. Série de Arquivos Abertos 13, Companhia Baiana de Recursos Minerais, Salvador pp 55
Magee CW, Palin JM, Taylor WR (2001) Laser ICP-MS analyses of detrital zircons from Proterozoic sediments in Bahia state, Brazil; implications for the evolution of the São Francisco craton prior to 3.3 Ga. Eleventh Annual V. M. Goldschmidt Conference, Hot Springs, Virginia, abstract no. 3501
McClay KR, Ellis PG (1983) Deformation and recrystallization of pyrite. Miner Mag 47:527–538
Meinhold G, Anders B, Kostopoulos D, Reichmann T (2008) Rutile chemistry and thermometry as provenance indicator: an example from Chios Island, Greece. Sedim Geol 203:98–111
Milesi JP, Ledru P, Marcoux E, Mourgeot R, Johan V, Lerouge C, Sabaté P, Bailly L, Respaut JP, Skipwith P (2002) The Jacobina Paleoproterozoic gold-bearing conglomerates, Bahia, Brazil: a "hydrothermal shear-reservoir" model. Ore Geol Rev 19:95–136
Minter WEL (1975) Sedimentological aspects of the Serra do Córrego Formation with particular reference to the Main Reef Unit at Cuzcuz and Morro do Vento near Jacobina, Bahia, Brazil. Unpubl Occasional Report File No.407/590, Anglo American Corp of South Africa Ltd, Welkom pp 20
Minter WEL (1999) Irrefutable detrital origin of the Witwatersrand gold and evidence of eolian signatures. Econ Geol 94:665–670
Minter WEL, Feather CE, Glathaar CW (1988) Sedimentological and mineralogical aspects of the newly discovered Witwatersrand placer deposit that reflect Proterozoic weathering, Welkom gold field, South Africa. Econ Geol 83:481–491
Minter WEL, Renger FE, Siegers A (1990) Early Proterozoic gold placers of the Moeda Formation within the Gandarela Syncline, Minas Gerais, Brazil. Econ Geol 85:943–951
Minter WEL, Goedhart ML, Knight J, Frimmel HE (1993) Morphology of Witwatersrand gold grains from the Basal Reef: evidence for their detrital origin. Econ Geol 88:237–248
Miranda DA, Misi A, Klein EL, Castro MP, Queiroga G (2021) A mineral system approach on the Paleoproterozoic Au-bearing quartz veins of the Jacobina Range, northeastern of the São Francisco Craton, Brazil. J South Am Earth Sci 103080
Molinari L, Scarpelli L (1988) Depositos de Ouro de Jacobina. Principais Depositos Minerais Do Brasil DNPM Brazil 3:463–478
Moreira IC, Oliveira EP, Martins de Sousa DF (2022) Evolution of the 3.65–2.58 Mairi Gneiss Complex, Brazil: implications for the growth of the continental crust in the São Francisco Craton. Geosci Front 13:101366
Mougeot R (1996) Étude de la limite Archéen-Protérozoïque et de minéralisations Au ± U associées. Exemple de la région de Jacobina, État de Bahia, et de Carajás, État de Pará, Brésil. Unpubl PhD thesis, Univ Montpellier II pp 301
Mougeot R, Marcoux E, Milesi JP, Ledru P, Johan V (1996) Geochemical and mineralogical characterizations of sulfide associated to the Jacobina gold mineralization Bahia, Brazil. XXXIX Anais do Congresso Brasileiro de Geologia, Salvador 7:318–320
Nutman AP, Cordani UG (1993) SHRIMP U-Pb zircon geochronology of Archaean granitoids from the Contendas-Mirante area of the Francisco Craton, Bahia, Brazil. Precamb Res 63:179–188
Oberthür T, Saager R (1986) Silver and mercury in gold particles from the Proterozoic Witwatersrand placer deposits of South Africa: metallogenic and geochemical implications. Econ Geol 81:20–31
Oliveira EP, McNaughton NJ, Zincone SA, Talavera C (2020) Birthplace of the São Francisco Craton, Brazil: evidence from 3.60 to 3.64 Ga gneisses of the Mairi Gneiss Complex. Terra Nova 32:281–289
Pape J, Mezger K, Robyr M (2016) A systematic evaluation of the Zr-in-rutile thermometer in ultra-high temperature (UHT) rocks. Contrib Mineral Petrol 171(44):2–20
Pearson WN, Tagliamonte PW (2005) An updated mineral resource and mineral reserve estimate and results of the 2004 exploration program for the Jacobina and Bahia Gold Belt property, Bahia State, Brazil. Desert Sun Mining Corporation (2005) U.S. Securities and Exchance Commision Archives 134 pp (https://www.sec.gov/Archives/edgar/data/1056086/000105291806000173/jacobinatechnicalreport.pdf)

Pearson WN, Macedo P M, Rubio A, Lorenzo C L, Karpeta P (2005) Geology and gold mineralization of the Jacobina Mine and Bahia Gold Belt, Bahia, Brazil, and a comparison to Tarkwa and Witwatersrand. Window to the World: 2005 Symposium Proceedings Geological Society of Nevada, Reno/Sparks Nevada, pp 757–785

Phillips GN, Myers RE (1989) The Witwatersrand Gold Fields: Part II. Origin for Witwatersrand gold during metamorphism and associated alteration. Econ Geol Monogr 6:598–608

Phillips GN, Law JDM (2000) Witwatersrand gold fields: geology, genesis, and exploration. Soc Econ Geol Rev 13:439–500

Putnis A (2009) Mineral replacement reactions. Rev Mineral Geochem 70:87–124

Ramdohr P (1955) Neue Beobachtungen an Erzen des Witwatersrandes in Südafrika und ihre genetische Bedeutung. Abh Akad Wiss Berlin Kl Math Allg Naturwiss 1954(5):43

Reid AM, le Roux AP, Minter WEL (1988) Composition of gold grains in the Vaal Placer, Klerksdorp, South Africa. Miner Deposita 23:211–217

Reis C et al (2021) Projeto Integração Geológica e Avaliação do Potencial Metalogenético da Serra de Jacobina e do Greenstone Belt de Mundo Novo. Informe de Recursos Minerais, Série Províncias Minerais do Brasil 31 CPRM pp 169

Saager R (1969) The relationship of silver and gold in the Basal Reef of the Witwatersrand System, South Africa. Miner Deposita 4:93–113

Saager R (1970) Structures in pyrite from the Basal Reef in the Orange Free State gold fields. Transact Geol Soc S Afr 73:29–46

Sabaté P, Marinho MM, Vidal P, Caen-Vachette M (1990) The 2-Ga peraluminous magmatism of the Jacobina-Contendas Mirante belts (Bahia, Brazil): geologic and isotopic constraints on the sources. Chem Geol 83:325–338

Santos D E (2011) Geologia e Geoquímica dos Corpos Máficos e Ultramáficos da Porção Sul da Serra de Jacobina, Cinturão de Ouro, Bahia. Unpubl BSc thesis, Universidade Federal de Sergipe pp 83

Soares ES, Lopes RG, Marsden H, Vasquez L Iturralde C, Bernier S (2020) NI 43–101 Technical Report Jacobina Gold Mine, Bahia State, Brazil. System for Electronic Document Analysis and Retrieval (SEDAR) Canadian Securities Administrator 190 pp http://s28.q4cdn.com/334653565/files/doc_downloads/Yamana-Jacobina-NI-43-101-May-29-2020.pdf

Strydom PM, Minter WEL (1976) A Stratigraphic and Sedimentological Report of the Main and Middle Reefs in the Itapecuru Prospect near Jacobina, Bahia, Brazil. Unpubl Occasional Report File No.407/590, Anglo American Corp of South Africa Ltd, Welkom pp 21

Teixeira JBG, de Souza JAB, da Silva MG, Leite CMM, Barbosa JSF, Coelho CES, Abram MB, Conceição Filho VM, Iyer SSS (2001) Gold mineralization in the Serra de Jacobina region, Bahia, Brazil: tectonic framework and metallogenesis. Miner Deposita 36:332–344

Teixeira JBG, da Silva MG, Misi A, Cruz SCP, Sá JHS (2010) Geotectonic setting and metallogeny of the northern São Francisco craton, Bahia, Brazil. J South Am Earth Sci 30:71–83

Teixeira JBG, Misi A, da Silva MG, Brito RSC (2019) Reconstruction of the Precambrian terranes of Northeastern Brazil along Cambrian strike-slip faults: a new model of geodynamic evolution and gold metallogeny in the State of Bahia. Braz J Geol 49(3):1–20

Teixeira LR (2017) Projeto ARIM – Serra de Jacobina: relatório temático de litogeoquímica. Relatório Interno CPRM, Salvador pp 28

Teles G, Chemale F Jr, Oliveira CG (2015) Paleoarchean record of the detrital pyrite-bearing, Jacobina Au-U deposits, Bahia, Brazil. Precamb Res 256:289–313

Teles GS, Chemale F Jr, Avila JN, Ireland TR, Dias ANC, Cruz DCF, Constantino CJL (2020) Textural and geochemical investigation of pyrite in Jacobina Basin, São Francisco Craton, Brazil: Implications for paleoenvironmental conditions and formation of pre-GOE metaconglomerate-hosted Au-(U) deposits. Geochim Cosmochim Acta 273:331–353

Tomkins HS, Powell R, Ellis DJ (2007) The pressure dependence of the zirconium-in-rutile thermometer. J Metamorphic Geol 25:703–713

Ulrich T, Long DGF, Kamber BS, Whitehouse MJ (2011) In situ trace element and sulfur isotope analysis of pyrite in a Paleoproterozoic gold placer deposit, Pardo and Clement townships, Ontario, Canada. Econ Geol 106:667–686

Utter T (1978) Morphology and geochemistry of different pyrite types from the Upper Witwatersrand System of the Klerksdorp Goldfield, South Africa. Geol Rdsch 67:774–804

Utter T (1979) The morphology and silver content of gold from the Upper Witwatersrand and Ventersdorp systems of the Klerksdorp Gold Field, South Africa. Econ Geol 74:27–44

Utter T (1980) Rounding of ore particles from the Witwatersrand gold and uranium deposit (South Africa) as an indicator of their detrital origin. J Sedim Petrol 50:71–76

Vidal O, Lanari P, Munoz M, Bourdelle F, Andrade V (2016) Deciphering temperature, pressure and oxygen-actively conditions of chlorite formation. Clays Miner 51:615–633

Von Gehlen K (1983) Silver and mercury in single gold grains from the Witwatersrand and Barberton, South Africa. Miner Deposita 18:529–534

Watson EB, Wark DA, Thomas JB (2006) Crystallization thermometers for zircon and rutile. Contrib Mineral Petrol 151:413–433

White MG (1956) Uranium in the auriferous conglomerates at the Canavieiras gold mine, State of Bahia, Brazil. Trace Element Memorandum Report 945, Division of Raw Materials US Atom Energy Comm, US Geol Surv pp 20

Youngson JH, Craw D (1999) Variation in placer style, gold morphology, and gold particle behavior down gravel bed-load rivers: an example from the Shotover/Arrow—Kawarau-Clutha river system, Otago, New Zealand. Econ Geol 94:615–634

Zack T, Kooijman E (2017) Petrology and geochronology of rutile. Rev Miner Geochem 83(1):443–467

Zack T, Moraes R, Kronz A (2004a) Temperature dependence of Zr in rutile: empirical calibration of a rutile thermometer. Contrib Mineral Petrol 148:471–488

Zack T, von Eynatten H, Kronz A (2004b) Rutile geochemistry and its potential use in quantitative provenance studies. Sediment Geol 171:37–58

Zane A, Weiss Z (1998) A procedure for classifying rock-forming chlorites based on microprobe data. Rend Fis Acc Lincei 9:51–56

Zang W, Fyfe WS (1995) Chloritization of the hydrothermally altered bedrock at the Igarapé Bahia gold deposit, Carajás, Brazil. Miner Deposita 30:30–38

Zeh A, Cabral AR, Koglin N, Decker M (2018) Rutile alteration and authigenic growth in the metasandstones of the Moeda Formation, Minas Gerais, Brazil – a result of Transamazonian fluid-rock interaction. Chem Geol 483:397–409

Zincone SA, Oliveira EP, Laurent O, Zhang H, Zhai M (2016) 3.30 Ga high-silica intraplate volcanic–plutonic system of the Gavião Block, São Francisco Craton, Brazil: evidence of an intracontinental rift following the creation of insulating continental crust. Lithos 266(267):414–434

Zincone SA, Barbuena D, Oliveira EP, Baldim MR (2017) Detrital zircon U-Pb ages as evidence for deposition of the Saúde Complex in a Paleoproterozoic foreland basin, northern São Francisco Craton, Brazil. J South Am Earth Sci 79:537–548